J. Fluid Mech. (1990), *vol.* 210, *pp.* 57–112
Printed in Great Britain

The decay of turbulence in thermally stratified flow

By J. H. LIENHARD V[1] AND C. W. VAN ATTA[2]†

[1] Department of Mechanical Engineering, Massachusetts Institute of Technology, Cambridge, MA 02139 USA

[2] Department of Applied Mechanics and Engineering Sciences, University of California at San Diego, La Jolla, CA 92093 USA

(Received 14 June 1988 and in revised form 7 June 1989)

The decay of grid-generated turbulence in the presence of strong thermal stratification is studied in a continuously stratified, open-loop wind tunnel at Brunt–Väisälä frequencies up to $2.5\,s^{-1}$. The data include one-point statistical measurements through moments of fourth order and associated power- and cross-spectra. Cross-channel phase measurements are used to analyse the scales of correlation of velocity and temperature. The present data are considerably more coherent than previous salt-stratified data, and the structural form of stratified turbulence is thus more clearly manifested. No internal wave effects are observed at any stage of the decay. Stratified turbulence is found to be a two-scale process dominated by buoyancy forces at large scales of motion and dissipative effects at small scales. The two-scale structure is used to develop universal buoyancy scalings for the decay of the vertical heat flux, the scalar variance, and the molecular dissipation rates, and, in particular, for the vertical velocity decay. Velocity and temperature spectra satisfy universal equilibrium scaling at high wavenumbers, but show buoyancy effects at small wavenumbers. The flow remains isotropic at high wavenumbers over the entire range of turbulent decay studied. Cospectral and phase data are used to validate the two-scale model of the turbulence. The flow may show large-scale restratification while active turbulence persists at smaller scales, so that the vanishing of the vertical transport does not represent extinction of turbulent motion. Additionally, an original universal equilibrium scaling is developed for the cross-spectrum. Lengthscale evolution is measured, and the overturning and buoyancy lengthscales (associated with potential and kinetic energy, respectively) are found to characterize flow development. The role of the Prandtl number is assessed by comparison to previous works, and the Prandtl number is found to have a significant influence upon stratified turbulence evolution.

1. Introduction

1.1. *Stratified grid turbulence experiments*

Turbulence in stratified media is a phenomenon common to a variety of geophysical and engineering situations. Oceanic and atmospheric microstructural transport, problems of environmental engineering, and a plethora of more specific subjects require an understanding of how turbulence can evolve in the presence of dynamically active buoyancy forces. At this time, much uncertainty remains as to the exact role of buoyancy forces in the dynamics of turbulent motion and scalar transport.

† Also Scripps Institution of Oceanography.

Previous investigations of strongly stratified turbulent flow have included both laboratory and field studies in steady and transient flows of salt-stratified water. Our interest is in grid turbulence experiments in stratified mean flows. A detailed review of the literature on stratified grid turbulence, up to 1985, is given by Itsweire, Helland, and Van Atta (1986), and here we shall focus on only those studies directly relevant to present considerations.

Such studies have been of two types: passively stratified wind tunnel studies and actively stratified salt-water tunnel studies. The air experiments to date have dealt exclusively with small temperature gradients for which buoyancy forces are negligible (Wiskind 1962; Montgomery 1974; Venkataramani & Chevray 1978; Sirivat & Warhaft 1983).

The actively stratified salt-water tunnel experiments have been conducted in a unique, continuous flow, salt-stratified water channel (Stillinger *et al.* 1983*a*; Stillinger, Helland & Van Atta 1983*b*). In addition to achieving the active stratifications not then available in air, these experiments offered many advantages over the earlier work in tow-tanks of Lin & Veenhuizen (1975), Dickey & Mellor (1980), Lange (1982), and Britter *et al.* (1983), notably the creation of steady sheared and unsheared flows which allowed more accurate statistical measurements.

Nevertheless, the salt-water tunnel experiments have had several shortcomings. Difficulties with high-accuracy instrumentation, mean profile unsteadiness, and the very small molecular scales of the scalar have made highly detailed information difficult to obtain. Another complication to the salt-water experiments is the presence of a strong internal wave field which hinders systematic interpretation of the measured velocity field.

These concerns motivate a change to experimentation in non-isothermal air flows. Much higher accuracy scalar and velocity measurements can be obtained by using air instead of water. The unsteadiness can be avoided by using a steadily heated, thermally stratified wind tunnel, as is done here. Moreover, such a tunnel can be designed so as to prevent undesirable standing internal waves in the test section.

An important difference between air and water experimentation lies in the values of the Prandtl number for air (0.71) and the Schmidt number for salt-water (~ 500). The small scales of the scalar are not unmeasurably tiny in non-isothermal air flows, which is to our advantage, but the differing behaviour of scalar diffusion will lead to more fundamental contrasts between the air and salt-water data. One objective of the present study, then, is to assess the role of the Prandtl number in stratified turbulence.

No previously published experimental work has treated the behaviour of strongly stratified turbulence in a continuously stratified air flow. In this work, we use a new facility which produces strong, linear temperature profiles in an open-loop wind tunnel to study the decay of grid turbulence in thermally stratified flow.

1.2. *Energy scales of stratified turbulence*

One of the major features of the present work is the manner in which the stratified turbulence is well characterized by its kinetic and potential energies. We begin with an analysis of the scales associated with these energies.

In a stratified medium of mean density $\bar{\rho}(z)$, with z the vertical coordinate and g the gravitational body force, the Brunt–Väisälä frequency, N, characterizes the level of stratification:

$$N = \left(-\frac{g}{\bar{\rho}} \frac{\partial \bar{\rho}}{\partial z} \right)^{\frac{1}{2}}. \tag{1}$$

Particles displaced from their positions of buoyant equilibrium, z_0, to another position, $\zeta+z_0$, experience a change in potential energy per unit volume given by

$$\Psi = -\tfrac{1}{2}g\zeta^2\left.\frac{\mathrm{d}\bar{\rho}}{\mathrm{d}z}\right|_{z_0} = \tfrac{1}{2}\bar{\rho}(z_0)\,\zeta^2 N^2. \tag{2}$$

If the stratified flow field is turbulent, the r.m.s. vertical kinetic energy of particles at level z_0 is

$$\bar{T} = \tfrac{1}{2}\bar{\rho}(z_0)\,\overline{w^2} \tag{3}$$

irrespective of the equilibrium levels of the particles which pass that level (since $\overline{\rho w^2} \approx \bar{\rho}\overline{w^2}$). These particles only have enough energy to travel vertically to an additional r.m.s. displacement ζ' at which they will have exchanged all of their kinetic energy for potential energy. The *buoyancy length*, L_b, is the r.m.s. vertical distance, ζ', that particles having the ambient r.m.s. kinetic energy can travel; from the preceding equations, it has the specific value

$$L_\mathrm{b} \equiv \left(\frac{w'}{N}\right). \tag{4}$$

This length describes the upper limit of the flow's ability to create additional potential energy, $\frac{1}{2}\bar{\rho}(z_0)N^2L_\mathrm{b}^2$. This limit is valid whether or not particles really travel the distance L_b.

If the temperature profile is of sufficiently small curvature that a linear distribution may be assumed, then the particle's displacement, $(z-z_0)$, from its equilibrium level, z_0, may be determined by measuring the temperature perturbation, $\theta = T(z)-T(z_0)$, which it produces. In a turbulent flow, the local r.m.s. displacement of fluid particles from their instantaneous equilibrium levels is found by measuring the local r.m.s. temperature fluctuation. This r.m.s. displacement is called the *overturning scale*, L_t, and is related to θ' by

$$L_\mathrm{t} = \frac{\theta'}{(\mathrm{d}\overline{T}/\mathrm{d}z)}. \tag{5}$$

The r.m.s. potential energy at any point z_0 is then

$$\bar{\Psi} = \tfrac{1}{2}\bar{\rho}(z_0)N^2L_\mathrm{t}^2. \tag{6}$$

The length L_t is thus a measure of the existing level of potential energy.

The two scales, L_b and L_t, are physical quantities, rather than scale estimates. Both are directly measurable from one-point ensemble averaging of w and θ (as elaborated for L_t below). Together they characterize the r.m.s. total (vertical) energy of the turbulence:

$$\bar{E} = \tfrac{1}{2}\bar{\rho}(z_0)N^2(L_\mathrm{b}^2+L_\mathrm{t}^2). \tag{7}$$

Equation (7) suggests that some relationship may exist between L_t and L_b. Certainly, in the flows we shall study, the turbulent kinetic energy serves to generate the turbulent potential energy; in this sense, L_b is a source of L_t and should prove to be an upper bound on it. In as much as L_b may be a physical limit on the size of the actual r.m.s. vertical displacement†, it may be true that $L_\mathrm{b} \geqslant L_\mathrm{t}$ at any instant.

Molecular diffusion of the stratifying scalar affects the potential energy described by L_t. Diffusion of heat will cause displaced fluid particles to approach the mean

† We avoid stating this as an exact result. The particle displacement model takes no account of the 'random' driving of the vertical displacement by the three-dimensional turbulent motion of the flow. The potential energy interpretation of L_b remains valid irrespective of the structure of the flow. Molecular diffusion will also be shown to influence the relation of L_b and L_t.

temperature of the surrounding fluid, lessening the buoyancy force they experience and destroying some portion of their potential energy. This change in the particle temperature is a reassignment of the particle's equilibrium level with respect to the temperature (density) gradient, from z_0 to the z at which the particle's new temperature equals $T(z)$. For this reason, the equilibrium levels of the particles are qualified as 'instantaneous' in the preceding remarks, rather than, say, 'initial'. With this qualifier, L_t retains its role in defining the r.m.s. turbulent potential energy, even in the face of significant molecular diffusion. The buoyancy length, L_b, is itself unaffected by molecular diffusion and continues to describe the instantaneous capacity of the flow to produce r.m.s. potential energy.

1.3. *Scales and parameters*

In this subsection, we describe the origins of the scalings to be employed and the mechanistic ideas behind the subsequent presentation of the results. The later sections of the paper examine the data from within this framework. While this approach is somewhat inverted (the data were collected before these models were constructed), it greatly simplifies the discussion of the results.

The fundamental phenomenon which differentiates the strongly stratified turbulent grid flow from other turbulent grid flows is the active role of buoyancy forces in suppressing the vertical migration of fluid particles. As a particle moves vertically, it loses kinetic energy to potential energy with respect to the density gradient. Some of this potential energy can be returned to kinetic energy if the particle moves (under the action of buoyancy forces, say) back toward its initial position in the density profile, but some of this energy will be lost to the molecular diffusion of the stratifying scalar.

A proper characterization of the flow requires some measure of the conversion of kinetic to potential energy, in addition to the measures which describe the initial scales, dissipation, and duration of the flow. The present data were found to be most clearly explained when the problem was viewed as depending upon two classes of parameters. In the first class are the usual variables of grid turbulence: the mesh size, M, the mean speed, U, the streamwise coordinate, x, or flow time, $t = x/U$, and the viscous dissipation, ϵ. The mesh size controls the initial scales of the turbulence, the flow time characterizes its history, the mean speed characterizes the magnitude of the turbulent velocity fluctuations (i.e. (16)), and the dissipation characterizes the small scales and the rate of decay.

In the second class are the parameters which characterize the action of buoyancy forces: the temperature (density) gradient, $\mathrm{d}T/\mathrm{d}z$, and the Brunt–Väisälä frequency, N, or a timescale associated with the action of buoyancy forces, such as $\tau = 2\pi/N$, the Väisälä period. The last of these may be combined with the flow time to form a non-dimensional group which reflects the relative time over which buoyancy effects are integrated by the flow: $t/\tau = xN/2\pi U$. The temperature gradient itself characterizes the magnitude of the turbulent temperature fluctuations. Specific forms of these scalings are developed below.

The turbulence under study has a fairly low Reynolds number; Re_λ ranges between 20 and 50 for the data presented here. Although this is not big enough that one might expect to observe an inertial subrange, it is still big enough that the large and small scales of the turbulence are well separated.

The small scales contribute most strongly to molecular dissipation (ϵ, χ), and the larger scales contribute to variance (u', w', θ') and transport ($\overline{w\theta}$), as described in §§3, 4, and 5. Since buoyancy effects are more severe for the larger-scale vertical motions,

we anticipate that the variance and transport quantities will be most affected by stratification, while the dissipation rates will be less affected. Consequently, the scaling of the data will attempt to separate small-scale effects – primarily viscous decay – from buoyancy effects.

This separation is actually somewhat surprising, since conventional wisdom tells us that the large scales of the flow fix the dissipation rates. Would not the dissipation rate be directly coupled to buoyancy influences on the large scales? We shall see that the explanation lies in the relative insensitivity of the horizontal turbulence components to buoyancy effects. The return-to-isotropy terms in the kinetic energy balance are weak, and the changes produced in the vertical motions do not greatly alter the overall flow of energy from large to small scales, so long as the flow retains the features of an active turbulence. A contrasting behaviour is found for the thermal dissipation rate (χ), which remains strongly dependent on the large-scale temperature variance. The temperature variance is in turn greatly affected by buoyancy forces because it arises only from the vertical migration of fluid particles – a migration which is suppressed by the density gradient.

The order of the presentation We first consider the various second-order moments and their balance equations. The velocity, scalar, and transport fields are discussed, and scalings are formulated which characterize their development in the presence of active buoyancy forces. This discussion uncovers the evolution of particle dispersion and the two-scale nature of the transport process and kinetic energy decay.

Using the information derived from these moments, a more structural explication of the convective transport is then built from the cross-spectrum of the heat flux. The cospectrum quantitatively illustrates the contribution of various scales to transport, and the phase shows specifically the degree of correlation of w and θ at each scale. That detailed information consolidates our presentation of stratified turbulence decay as a distinctly two-scale process. From this vantage point, the various lengthscales thought to characterize stratified turbulent flow are scrutinized, and the possible influences of internal waves and the Prandtl number are examined.

1.4. *The experimental facility*

The stratified-flow wind tunnel (figure 1) has been described by Lienhard & Van Atta (1989). The incoming air flow is electrically heated upstream of the contraction at the test-section inlet. A biplane grid is placed between the outlet of the contraction and the entrance of the test section. The facility is capable of developing linear stratifications of up to 200 °C/m (Väisälä frequencies of 2.5 s^{-1}) at uniform mean speed in the range of 2–5 m/s.

The test section has an overall length of 4.9 m, with vertical walls at an interior separation of 57.8 cm. The floor and ceiling of the test section are separated by 30.5 cm at the inlet and gradually diverge downstream at a rate chosen to remove the streamwise pressure gradient associated with wall boundary-layer growth. The ceiling of the test section is covered with fibreglass insulation. Two stainless steel grids were employed, a 2.54 cm mesh and a 5.08 cm mesh. Both had a solidity of 34.0%.

1.4.1. *Instrumentation*

Simultaneous measurements of streamwise and vertical velocities, u and w, and of fluctuating temperature, θ, were obtained using thermal anemometry, accounting for large temperature variations in interpreting the sensor response. The output voltage,

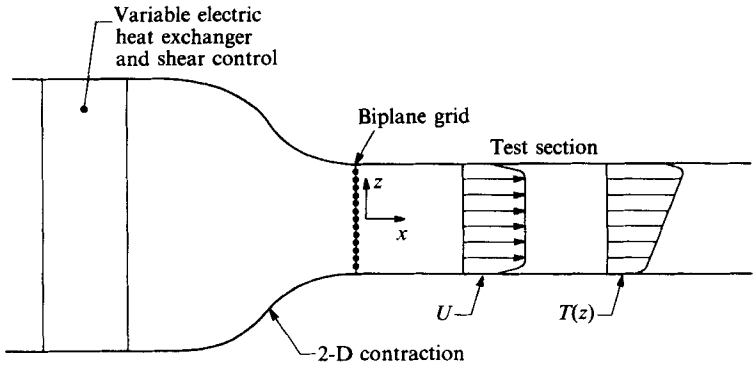

FIGURE 1. The heat exchanger, final contraction, and test section of the thermally stratified wind tunnel.

E_0, of a constant-temperature hot-wire anemometer is accurately represented as a function of sensor temperature, T_w, air temperature, T, and flow speed, U, by

$$E_0^2 = (T_w - T)\,(A(T_w + T)^{0.84} + BU^{0.45}). \tag{8}$$

As usual, the temperature difference factor accounts for variations in the heat transfer driving force, and the temperature sum factor accounts for thermal property variations. The appropriate values of A, B, and T_w are found for each sensor by a calibration.

An $\times$-wire and adjacent cold wire were used in conjunction with (8) to obtain the desired measurements. The cold wire provides the instantaneous air temperature. The output voltage of each channel of the $\times$-wire then yields u and w from (8) and a pitching calibration. The velocity sensor was a Dantec 55P61 $\times$-wire probe: platinum sensor diameter of 5 μm; sensor length of 1.25 mm; sensor separation of 1.0 mm. The temperature sensor was a Dantec 55P31 resistance thermometer probe: platinum sensor diameter of 1.0 μm; sensor length of 0.4 mm. The $\times$-wire was aligned with the mean flow direction with its sensors lying in vertical planes; the cold-wire sensor, also lying in a vertical plane, was then brought to within 1 mm of the nearest $\times$-wire sensor. The overall sampling volume was smaller than $1 \times 1 \times 2$ mm, with the largest dimension in the transverse (y) direction.

The low speeds of the present flows maintained fairly large Kolomogorov and Corrsin scales, which allowed accurate resolution of both viscous and scalar dissipation rates. Representative scalar dissipation spectra are shown in §4. The spatial and temporal resolution of the probe array is discussed at length by Lienhard (1988).

The overheat ratios on the constant-temperature anemometers were set at 1.95 for all runs herein, giving wire temperatures of 270–280 °C. These high operating temperatures were chosen to reduce the temperature sensitivity of the hot wires. Tests made in isothermal turbulent jets indicated that no contamination of the cold-wire signal by the thermal wakes of the hot wires occurred for r.m.s. turbulent intensities of less than about 20%. The present grid data had intensities on the order of only 8% or less.

The effective wire temperature, T_w, was taken as that which best correlated the calibration data according to (8). Estimated uncertainties in the values so obtained were generally less than ± 3 °C. Numerical tests indicated that the statistical data

were not significantly affected (changes of 5% or less in the non-zero cross-channel statistics) by errors in T_w as large as ± 10 °C.

The amplifier outputs were low-pass filtered to prevent aliasing. The experimental time series were recorded for subsequent data reduction. Additional details of the measurement, recording, and reduction procedure are given by Lienhard (1988).

1.4.2. *Velocity and temperature profiles*

The velocity profile was uniform at the entrance of the test section. No shear could be measured at the outlet of the contraction, and the residual velocity turbulence ($u'/U = 0.5\%$) was entirely eradicated by the grid.

Linear mean temperature profiles were found corresponding to a number of Väisälä frequencies and mean speeds of 2.0 m/s and 2.5 m/s. The temperature profiles could generally be set so that no point measured deviated from the linear distribution by more than 0.3 °C for the weakly stratified profiles or by more than 1 °C for the strongly stratified profiles. The r.m.s. error in the mean profiles is considerably smaller. Profiles can be held indefinitely, after an initial warming transient of about one hour.

The flow entering the test section had low-frequency (< 100 Hz) temperature noise (± 0.36 °C at $N = 2.1\ s^{-1}$), arising both from the non-uniformity of the heat exchanger and from other upstream mixing processes; consequently, the temperature gradients for a given size grid must produce initial temperature fluctuations sufficient to eradicate this noise. Thus, the 2.54 cm mesh grid was used only for $N \geqslant 1.60\ s^{-1}$ and the 5.08 cm mesh for $N \geqslant 1.16\ s^{-1}$.

The measurements showed no significant wall downflow and no consistent skewing of the temperature profile which might signal the presence of large-scale natural convection. The horizontal non-uniformities seen in the mean temperature profiles were also small compared with the level of vertical stratification, and the flow may reasonably be treated as if it possesses only a uniform vertical temperature gradient.

A related question is whether an internal wave field might be generated within the test section, distorting the mean profiles in the tunnel. Analysis of such two-dimensional, standing waves shows that they are not possible unless the modified Froude number, $Fr_m^2 = (U/NH)^2$, is less than $1/\pi^2$, for a constant mean speed U and test-section height H. Since the test flow always has an internal Froude number greater than about 2.6, it is always supercritical with respect to two-dimensional standing internal waves. Another potential cause of standing internal waves is the passage of the stratified flow through the contraction at the tunnel inlet. A similar analysis shows that these flows are also supercritical to waves of that type.

Moments of the velocity up to fourth order were measured along a transverse cross-section of the tunnel to map out what portion of the flow remained uncontaminated by the wall boundary layers. The dimensions of the uncontaminated core are about 16 cm by 38 cm at 3.4 m from the grid. The region of wall temperature contamination was essentially identical. The test flow remains at a uniform speed and shows isotropic turbulent behaviour throughout the test section within the core region.

A flow-mapping experiment with the 2.54 cm grid shows that the homogeneity of the r.m.s. velocity components is 6–9% throughout the wall-independent regions of the test section. The convective heat flux correlation coefficient, $\overline{w\theta}/w'\theta'$, and the Reynolds stress correlation coefficient, $\overline{uw}/u'w'$, show deviations from homogeneity (away from wall-influenced regions) of about 13% and 10%, respectively. The temperature fluctuation, θ', is initially homogeneous to an r.m.s. deviation of 16%

	x/M	t/τ	U (m/s)	T (°C)	u' (cm/s)	w' (cm/s)	θ' (°C)	$-\frac{\overline{w\theta}}{w'\theta'}$	ϵ (m²/s³)	χ (°C²/s)	Co	η (mm)	η_0 (mm)	L_t (mm)	L_b (mm)	L_O (mm)
A**	6.8	0.063	2.111	51.5	16.78	15.43	1.33	0.547	0.373	17.48	8.69	0.357	0.463	6.73	63.78	162.1
A	9.1	0.085	2.099	52.0	13.09	11.82	1.43	0.563	0.193	16.71	8.31	0.421	0.546	7.23	48.83	116.6
B	11.9	0.112	2.082	52.2	10.18	8.87	1.66	0.590	0.0888	15.80	7.86	0.511	0.663	8.40	36.66	79.14
C	16.9	0.158	2.085	52.7	7.71	6.42	1.78	0.600	0.0382	13.23	6.58	0.631	0.818	9.02	26.52	51.91
D	22.2	0.205	2.121	53.5	6.38	4.97	1.82	0.590	0.0194	10.44	5.19	0.748	0.969	9.20	20.54	36.96
E′	26.1	0.240	2.122	53.8	5.56	4.01	1.85	0.554	0.0104	9.02	4.59	0.874	1.132	9.36	16.56	27.10
E	29.6	0.273	2.118	54.2	4.89	3.43	1.85	0.511	0.00801	8.03	3.99	0.933	1.209	9.38	14.19	23.78
F′	34.4	0.323	2.089	55.0	4.22	2.69	1.80	0.423	0.00454	6.47	3.22	1.075	1.393	9.11	11.14	17.91
F	37.2	0.348	2.093	55.1	3.99	2.44	1.80	0.352	0.00355	5.82	2.89	1.144	1.482	9.12	10.10	15.83
G′	44.3	0.408	2.124	53.5	3.41	2.02	1.68	0.153	0.00191	4.07	2.03	1.335	1.729	8.52	8.33	11.62
G	48.8	0.447	2.140	53.8	3.15	1.92	1.58	0.093	0.00144	3.33	1.66	1.433	1.856	7.99	7.92	10.08
H′	54.8	0.505	2.121	53.8	2.87	1.84	1.41	−0.007	0.000998	2.32	1.15	1.570	2.034	7.16	7.61	8.39
H	58.1	0.536	2.121	53.6	2.90	1.81	1.34	−0.016	0.000852	2.03	1.01	1.633	2.116	6.78	7.47	7.75
I′	62.3	0.578	2.110	53.1	2.64	1.78	1.25	−0.016	0.000676	1.62	0.805	1.731	2.243	6.35	7.37	6.91
I	66.4	0.619	2.099	52.9	2.58	1.74	1.18	0.025	0.000570	1.33	0.659	1.806	2.340	5.98	7.20	6.34
J′	70.6	0.665	2.078	52.7	2.55	1.69	1.11	0.087	0.000380	1.01	0.502	1.999	2.590	5.62	7.00	5.18
J	75.2	0.710	2.071	52.6	2.40	1.60	1.08	0.129	0.000367	0.856	0.426	2.017	2.612	5.47	6.63	5.09
K′	82.5	0.784	2.058	52.2	2.41	1.49	1.03	0.176	0.000281	0.665	0.331	2.157	2.794	5.21	6.15	4.45

TABLE 1. Compendium of data from the eighteen measuring stations for $N = 2.42\ s^{-1}$ and $M = 5.08$ cm

	x/M	t/τ	U (m/s)	T (°C)	u' (cm/s)	w' (cm/s)	θ' (°C)	$-\overline{w\theta}/w'\theta'$	ϵ (m²/s³)	χ (°C²/s)	Co	η (mm)	η_θ (mm)	L_t (mm)	L_b (mm)	L_O (mm)
A**	6.8	0.051	2.329	51.2	19.00	16.64	1.00	0.540	0.590	13.64	10.73	0.319	0.413	6.37	76.70	240.3
A	9.1	0.067	2.394	51.2	15.35	13.43	1.12	0.573	0.323	13.24	10.42	0.371	0.480	7.11	61.90	177.8
B	11.9	0.086	2.420	51.2	12.16	10.56	1.26	0.602	0.160	12.73	10.01	0.442	0.572	8.06	48.65	125.0
C	16.9	0.122	2.429	51.7	9.34	7.88	1.36	0.619	0.0690	10.50	8.26	0.544	0.706	8.65	36.29	82.14
D	22.2	0.162	2.410	52.4	7.41	5.96	1.42	0.626	0.0312	8.49	6.68	0.664	0.860	9.05	27.45	55.30
E′	26.1	0.190	2.406	52.8	6.47	5.04	1.46	0.618	0.0195	7.49	5.90	0.747	0.968	9.29	23.22	43.69
E	29.6	0.217	2.391	53.3	5.80	4.30	1.49	0.597	0.01303	6.76	5.32	0.826	1.071	9.50	19.82	35.71
F′	34.4	0.252	2.401	53.9	5.35	3.67	1.51	0.566	0.00850	5.91	4.65	0.920	1.191	9.62	16.90	28.83
F	37.2	0.272	2.404	53.9	4.79	3.33	1.52	0.545	0.00685	5.59	4.40	0.970	1.258	9.68	15.36	25.89
G′	44.3	0.321	2.420	52.9	4.14	2.68	1.55	0.452	0.00400	4.68	3.69	1.110	1.439	9.88	12.35	19.78
G	48.8	0.350	2.449	53.2	4.11	2.47	1.52	0.405	0.00255	3.71	2.92	1.242	1.609	9.65	11.39	15.81
H′	54.8	0.395	2.433	53.7	3.72	2.16	1.46	0.305	0.00223	3.41	2.69	1.285	1.664	9.27	9.94	14.77
H	58.1	0.419	2.434	53.6	3.49	2.06	1.42	0.258	0.00193	3.16	2.48	1.331	1.725	9.06	9.47	13.76
I′	62.3	0.451	2.424	53.7	3.35	1.94	1.39	0.182	0.00161	2.88	2.26	1.394	1.806	8.88	8.92	12.55
I	66.4	0.481	2.425	53.7	3.27	1.87	1.35	0.123	0.00136	2.53	1.99	1.454	1.883	8.58	8.62	11.55
J′	70.6	0.517	2.396	53.8	3.26	1.80	1.29	0.045	0.00111	2.13	1.67	1.530	1.983	8.24	8.31	10.42
J	75.2	0.563	2.343	54.0	3.00	1.73	1.19	0.016	0.000868	1.74	1.37	1.627	2.107	7.60	7.96	9.22
K′	82.5	0.613	2.360	53.9	2.72	1.74	1.12	−0.019	0.000675	1.38	1.09	1.732	2.245	7.13	8.01	8.13

TABLE 2. $N = 2.17\ \text{s}^{-1}$ and $M = 5.08$ cm

	x/M	t/τ	U (m/s)	T (°C)	u' (cm/s)	w' (cm/s)	θ' (°C)	$-\overline{w\theta}/w'\theta'$	ϵ (m²/s³)	χ (°C²/s)	Co	η (mm)	η_θ (mm)	L_t (mm)	L_b (mm)	L_O (mm)
A**	6.8	0.033	2.487	37.8	19.79	17.75	0.424	0.541	0.588	2.105	8.43	0.302	0.391	5.86	119.1	421.7
A	9.1	0.044	2.513	37.9	15.93	14.12	0.508	0.573	0.314	2.483	9.94	0.353	0.458	7.03	94.74	307.8
B	11.9	0.056	2.537	38.1	12.39	10.97	0.595	0.611	0.147	2.577	10.32	0.427	0.552	8.24	73.64	211.1
C	16.9	0.080	2.551	38.4	9.53	8.30	0.682	0.632	0.0647	2.491	9.97	0.524	0.679	9.45	55.72	139.8
D	22.2	0.106	2.524	38.9	7.57	6.44	0.745	0.644	0.0293	2.178	8.72	0.639	0.827	10.32	43.24	94.12
E′	26.1	0.127	2.467	39.3	6.45	5.40	0.802	0.649	0.0176	2.106	8.43	0.726	0.939	11.10	36.24	72.84
E	29.6	0.144	2.472	39.4	5.92	4.81	0.836	0.644	0.0124	1.939	7.76	0.792	1.024	11.57	32.25	61.24
F′	34.4	0.170	2.440	40.0	5.14	3.98	0.871	0.623	0.00738	1.756	7.03	0.902	1.167	12.06	26.70	47.22
F	37.2	0.183	2.447	40.0	4.84	3.71	0.871	0.619	0.00611	1.703	6.82	0.945	1.223	12.06	24.88	42.97
G′	44.3	0.220	2.429	39.7	4.20	3.06	0.893	0.581	0.00363	1.436	5.75	1.076	1.393	12.36	20.51	33.12
G	48.8	0.241	2.443	39.7	4.06	2.78	0.889	0.551	0.00288	1.293	5.18	1.142	1.477	12.31	18.64	29.50
H′	54.8	0.273	2.421	39.8	3.62	2.38	0.880	0.494	0.00202	1.156	4.63	1.246	1.613	12.29	15.99	24.70
H	58.1	0.289	2.425	39.9	3.52	2.24	0.892	0.461	0.00175	1.083	4.34	1.292	1.672	12.34	15.04	23.03
I′	62.3	0.308	2.441	39.9	3.38	2.11	0.870	0.422	0.00147	0.974	3.90	1.350	1.746	12.04	14.13	21.09
I	66.4	0.331	2.421	39.9	3.21	1.95	0.859	0.365	0.00122	0.897	3.59	1.415	1.831	11.88	13.11	19.16
J′	70.6	0.354	2.402	40.2	3.04	1.83	0.844	0.305	0.00103	0.829	3.32	1.474	1.908	11.68	12.28	17.66
J	75.2	0.389	2.329	40.2	2.88	1.66	0.822	0.229	0.000802	0.727	2.91	1.571	2.033	11.38	11.16	15.58
K′	82.5	0.419	2.375	40.4	2.78	1.62	0.785	0.150	0.000627	0.604	2.42	1.670	2.162	10.86	10.87	13.78

TABLE 3. $N = 1.49\ \text{s}^{-1}$ and $M = 5.08$ cm

	x/M	t/τ	U (m/s)	T (°C)	u' (cm/s)	w' (cm/s)	θ' (°C)	$-\overline{w\theta}/w'\theta'$	ϵ (m²/s³)	χ (°C²/s)	Co	η (mm)	η_θ (mm)	L_t (mm)	L_b (mm)	L_O (mm)
A**	6.8	0.026	2.469	29.1	19.16	17.47	0.311	0.549	0.518	1.087	14.15	0.298	0.385	7.53	150.6	575.9
A	9.1	0.035	2.458	29.1	15.25	13.75	0.362	0.571	0.276	1.201	15.64	0.349	0.450	8.75	118.5	420.5
B	11.9	0.046	2.442	29.2	11.53	10.38	0.401	0.602	0.123	1.132	14.73	0.426	0.551	9.70	89.5	280.8
C	16.9	0.065	2.447	29.5	8.91	7.84	0.449	0.627	0.0516	1.006	13.09	0.530	0.685	10.86	67.6	181.8
D	22.2	0.083	2.455	30.0	7.21	6.25	0.484	0.643	0.0260	0.875	11.39	0.629	0.813	11.72	53.9	129.0
E′	26.1	0.099	2.455	30.1	6.44	5.46	0.508	0.651	0.0164	0.807	10.51	0.705	0.912	12.29	47.1	102.6
E	29.6	0.113	2.462	30.2	5.83	4.87	0.520	0.655	0.0114	0.744	9.68	0.773	0.999	12.57	42.0	85.4
F′	34.4	0.130	2.482	30.3	5.25	4.28	0.533	0.649	0.00773	0.663	8.62	0.852	1.101	12.90	36.9	70.4
F	37.2	0.141	2.480	30.4	4.95	3.99	0.544	0.649	0.00634	0.637	8.29	0.895	1.157	13.16	34.4	63.7
G′	44.3	0.168	2.477	30.0	4.38	3.38	0.556	0.627	0.00338	0.567	7.38	1.048	1.354	13.45	29.1	46.6
G	48.8	0.185	2.481	30.1	4.11	3.08	0.555	0.613	0.00310	0.513	6.67	1.071	1.384	13.42	26.6	44.6
H′	54.8	0.211	2.437	30.2	3.90	2.68	0.552	0.572	0.00217	0.456	5.93	1.171	1.513	13.35	23.1	37.2
H	58.1	0.223	2.448	30.2	3.60	2.55	0.560	0.561	0.00191	0.436	5.67	1.208	1.561	13.54	22.0	35.0
I′	62.3	0.242	2.417	30.2	3.59	2.33	0.559	0.538	0.00155	0.399	5.19	1.274	1.646	13.53	20.1	31.5
I	66.4	0.259	2.410	30.2	3.31	2.18	0.560	0.511	0.00129	0.382	4.97	1.334	1.724	13.56	18.8	28.7
J′	70.6	0.276	2.397	30.2	3.08	2.03	0.548	0.468	0.00110	0.351	4.57	1.386	1.791	13.27	17.5	26.6
J	75.2	0.299	2.359	30.4	2.95	1.87	0.549	0.436	0.000899	0.335	4.36	1.459	1.886	13.27	16.2	24.0
K′	82.5	0.336	2.300	30.5	2.65	1.63	0.537	0.345	0.000619	0.285	3.71	1.602	2.070	13.00	14.0	19.9

TABLE 4. $N = 1.16\ \mathrm{s}^{-1}$ and $m = 5.08$ cm

	x/M	U (m/s)	u' (cm/s)	w' (cm/s)	ϵ (m^2/s^3)	η (mm)
A**	6.8	2.383	19.01	16.73	0.469	0.294
A	9.1	2.413	15.17	13.42	0.249	0.345
B	11.9	2.431	11.78	10.47	0.119	0.415
C	16.9	2.429	8.76	7.95	0.0480	0.520
D	22.2	2.365	6.87	6.16	0.0214	0.637
E′	26.1	2.349	6.07	5.42	0.0137	0.712
E	29.6	2.355	5.50	4.89	0.00986	0.773
F′	34.4	2.344	4.87	4.32	0.00637	0.863
F	37.2	2.361	4.65	4.11	0.00532	0.902
G′	44.3	2.331	4.12	3.57	0.00328	1.018
G	48.8	2.331	3.87	3.37	0.00240	1.101
H′	54.8	2.317	3.48	3.09	0.00197	1.156
H	58.1	2.320	3.39	2.97	0.00175	1.191
I′	62.3	2.310	3.27	2.85	0.00153	1.232
I	66.4	2.261	3.08	2.66	0.00130	1.284
J′	70.6	2.288	3.04	2.60	0.00113	1.328
J	75.2	2.259	2.87	2.45	0.000977	1.378
K′	82.5	2.218	2.68	2.25	0.000747	1.474

TABLE 5. $N = 0.0\ s^{-1}$ and $M = 5.08$ cm

	x/M	t/τ	U (m/s)	T (°C)	u' (cm/s)	w' (cm/s)	θ' (°C)	$-\frac{\overline{w\theta}}{w'\theta'}$
A**	13.6	0.047	2.572	50.7	10.26	9.10	0.697	0.601
A	18.3	0.062	2.566	50.9	7.94	7.05	0.763	0.650
B	23.8	0.081	2.573	51.0	6.35	5.40	0.840	0.656
C	33.8	0.115	2.574	51.5	4.90	3.96	0.863	0.666
D	44.4	0.149	2.612	51.9	4.20	3.23	0.883	0.660
E′	52.1	0.174	2.624	52.2	3.68	2.78	0.910	0.643
E	59.1	0.193	2.683	51.9	3.51	2.53	0.903	0.628
F′	68.9	0.223	2.715	52.3	3.19	2.17	0.948	0.597
F	74.4	0.237	2.752	52.4	3.08	2.08	0.967	0.597
G′	88.6	0.279	2.786	52.1	3.33	1.70	0.961	0.477
G	97.6	0.307	2.788	52.8	2.54	1.56	0.945	0.440
H′	109.5	0.351	2.736	53.4	2.31	1.33	0.931	0.377
H	116.1	0.373	2.730	53.9	2.30	1.27	0.905	0.343
I′	124.6	0.407	2.690	53.9	2.24	1.18	0.883	0.249
I	132.9	0.433	2.692	53.9	2.12	1.14	0.853	0.200
J′	141.3	0.463	2.678	54.4	2.10	1.09	0.805	0.101
J	150.4	0.495	2.668	54.7	1.94	1.08	0.796	0.084
K′	165.0	0.549	2.635	54.6	1.86	1.08	0.753	−0.043

TABLE 6. $N = 2.17\ s^{-1}$ and $M = 2.54$ cm

for this grid. This variation is not prohibitively inhomogeneous and decreases downstream, reaching a level of only about 9%. Moreover, the larger grid (5.08 cm mesh) used for the bulk of the following data produces larger temperature disturbances which show less scatter than the small grid used in the mapping experiment; statistics presented below are also based on 200 records, rather than 50

	x/M	U (m/s)	u' (cm/s)	w' (cm/s)	ϵ (m^2/s^3)	η (mm)
A**	13.6	2.488	10.07	8.57	0.149	0.392
A	18.3	2.494	7.77	6.64	0.0649	0.483
B	23.8	2.493	6.10	5.29	0.0243	0.617
C	33.8	2.507	4.75	4.01	0.0119	0.737
D	44.4	2.487	3.87	3.37	0.00597	0.877
E′	52.1	2.491	3.51	3.01	0.00410	0.963
E	59.1	2.500	3.25	2.78	0.00302	1.039
F′	68.9	2.487	2.93	2.47	0.00206	1.144
F	74.4	2.464	2.86	2.34	0.00170	1.201
G′	88.6	2.431	2.47	2.06	0.00112	1.331
G	97.6	2.449	2.36	1.92	0.000917	1.400
H′	109.5	2.429	2.20	1.81	0.000712	1.492
H	116.1	2.427	2.18	1.72	0.000622	1.543
I′	124.6	2.424	2.08	1.68	0.000537	1.601
I	132.9	2.424	1.99	1.62	0.000470	1.655
J′	141.3	2.419	1.93	1.57	0.000411	1.711
J	150.4	2.403	1.87	1.55	0.000370	1.758
K′	165.0	2.383	1.78	1.44	0.000302	1.849

TABLE 7. $N = 0.0\ s^{-1}$ and $M = 2.54$ cm

records in the flow mapping. Additional information on the facility performance is given by Lienhard & Van Atta (1989) and by Lienhard (1988).

1.4.3. *The measurements*

Measurements were made at eighteen stations along the centreline of the stratified-flow wind tunnel. Each station was assigned a reference letter according to its distance from the grid. Data were acquired for the two grid sizes and a variety of stratifications. All runs had a mean speed of about 2.5 m/s, with the exception of the two highest-stratification runs ($N = 2.42\ s^{-1}$, $M = 5.08$ cm; $N = 2.51\ s^{-1}$, $M = 2.54$ cm), which had mean speeds of about 2.0 m/s. A compendium of data is given in tables 1–7. The microscale Reynolds number was about 30 for the large grid data and about 20 for the small grid.

At each station, 200 records of data were recorded at 4096 samples per record with a sample rate of 2048 samples per second. These measurements provide the bulk of the data considered herein. At stations C, G, and J′, 100 data records were recorded at 4096 samples per record with a sample rate of 256 samples per second. The latter measurements were used to examine the low-frequency content of the turbulence signals.

2. Convective heat fluxes

We have direct measurements of two components of the convective heat flux vector which we shall characterize in terms of the velocity–temperature correlations:

$$\overline{u\theta} = \frac{q_x}{\rho c_p}, \quad \overline{w\theta} = \frac{q_z}{\rho c_p}, \tag{9}$$

for c_p the specific heat at constant pressure and ρ the local density. The magnitude of these correlations depends not only upon the extent to which temperature

fluctuations are in phase with velocity fluctuations, but also upon the magnitude of the turbulent motions as characterized by u', w', and θ'. A direct measure of the efficiency of a turbulent flow in transporting heat, independent of the magnitude of turbulent fluctuations, may be obtained by normalizing the velocity–temperature correlations with the r.m.s. values to obtain the correlation coefficients:

$$\frac{\overline{w\theta}}{w'\theta'}, \quad \frac{\overline{u\theta}}{u'\theta'}. \tag{10}$$

In this section, buoyancy effects on the heat flux correlations are considered.

2.1. *Vertical convective heat flux*

From an engineering and geophysical point of view, the vertical heat transport is the most important quantity measured in this flow. Our interest is in the effect that stable stratification may have upon the ability of the turbulence to carry heat down the temperature gradient. We anticipate that the stratification, in suppressing the vertical migration of fluid particles, will suppress the vertical transport of heat.

Figure 2(*a*) shows the vertical convective heat flux correlation coefficient for two different grid sizes and six different stratifications as a function of the downstream position, x/M. The various curves have more or less the same initial value followed by decay at rates which vary with the level of stratification. The role of N in controlling these decay rates is not accounted by the scaling of $\overline{w\theta}$ with w' and θ', but we may accommodate such variations of N by rescaling the abscissa in terms of the buoyancy time, t/τ, as in figure 2(*b*).

The unambiguous collapse of the buoyancy-scaled data onto a single curve illustrates that buoyant reduction of the vertical heat transport is indeed directly proportional to the elapsed buoyancy-scaled time. The heat flux correlation coefficient shows no discernible dependence upon the viscous decay of the flow or the local intensity of the turbulence, nor any effects of the mesh and microscale Reynolds numbers: these parameters are all carried by the normalization of the heat flux with w' and θ'. The effect of the Väisälä frequency is entirely carried by its appearance in the non-dimensional time; this is another reflection of the scaling of the heat flux with θ'. However, the degradation of $\overline{w\theta}/w'\theta'$ as t/τ increases demonstrates the marked reduction of the flow's heat transfer efficiency caused by buoyancy forces.

For comparison to experiments which study so-called 'passive stratification', we may divide the heat flux correlation coefficient history into two regions. For t/τ less than about 0.1, $\overline{w\theta}/w'\theta'$ changes little in time, apart from a slight growth which might simply be attributed to the proximity of the turbulence to the grid. In this small region, buoyancy forces have no real influence on the flow, and the stratification might be considered to be 'passive'. In the second region, for t/τ greater than 0.1 or so, buoyancy forces play an active role in a flow's dynamics. From figure 2 we see that there is really no such thing as passive stratification, only stratified turbulence that is not allowed to evolve so long that buoyancy effects become pronounced.

For our flows, $\overline{w\theta}/w'\theta'$ is in the range of -0.60 to -0.65 in the passive region, neglecting the first few points which are surely still evolving. These values compare favourably to the passively stratified air flow measurements of other investigators (see §7.2). Conversely, for the actively stratified grid turbulence experiments in salt water (Stillinger *et al.* 1983*b*; Itsweire *et al.* 1986), the vertical transport correlation coefficient never exceeded 0.45, and often had maximum values of only 0.35. As developed in later sections, this contrast almost certainly results from the great

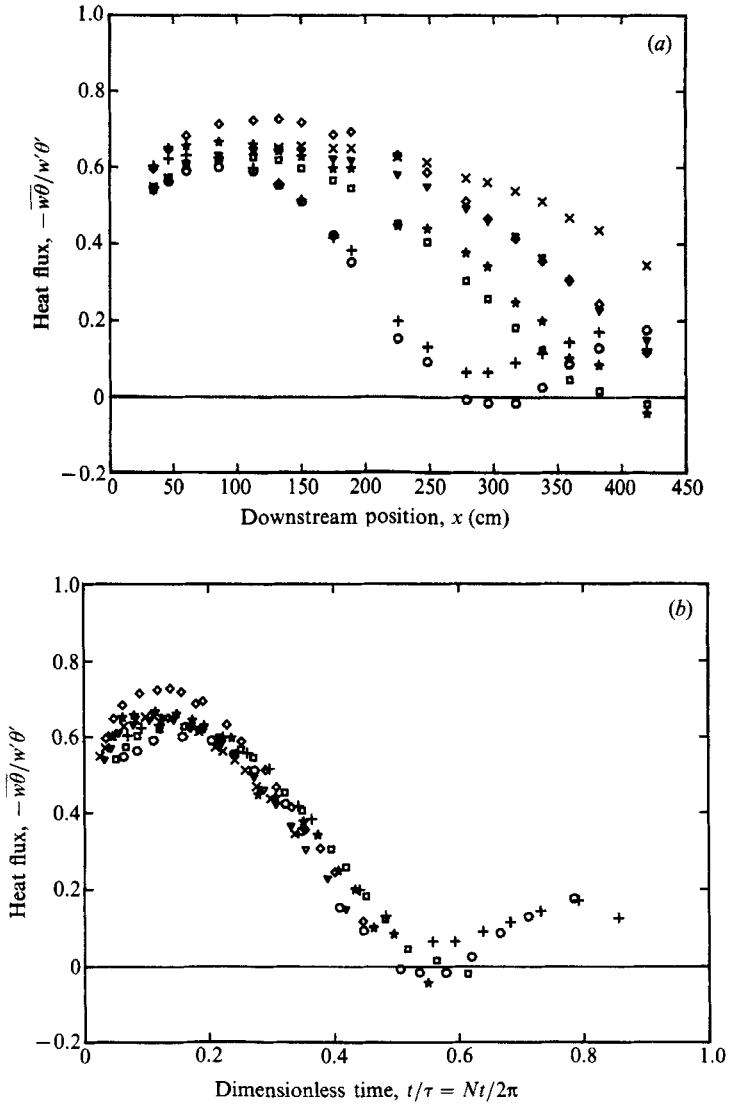

FIGURE 2. The effect of stratification on the vertical transport of heat, (*a*) as a function of streamwise position, x, (*b*) as a function of buoyancy time, t/τ. $M = 5.08$ cm: ○, $N = 2.42$ s^{-1}; □, $N = 2.17$ s^{-1}; ▽, $N = 1.49$ s^{-1}; ×, $N = 1.16$ s^{-1}. $M = 2.54$ cm: +, $N = 2.51$ s^{-1}. ★. $N = 2.17$ s^{-1}; ◇. $N = 1.60$ s^{-1}.

difference in the sizes of the Prandtl number here and the Schmidt number there, which affects the relative strengths of turbulent and molecular transport (see §7.5).

The collapse of the heat flux beyond the passive region may be explained in terms of the declining vertical kinetic energy of the flow. As the flow decays under viscous influences, fluid particles have less kinetic energy to exchange for potential energy in their vertical motions. This is particularly significant for the larger-scale motions which involve greater gains of potential energy. As a result, vertical travel is retarded for those motions that might sustain a high level of scalar variance. Moreover, the kinetic energy is no longer sufficient to support the mixed state of the flow, and particles which were vertically dispersed during the earlier more vigorous turbulence

now begin to drift back toward their buoyant equilibrium positions in the density profile. This restratification process also primarily affects the large scales.

From these considerations, we obtain a picture of the buoyancy-influenced transport as one in which the large-scale motions not only cease to actively transport heat down the temperature gradient, but may also carry heat counter to the temperature gradient by virtue of the restratification process. The small-scale motions, however, can continue to mix actively. Hence, the structure of the vertical transport now differs markedly from that in the initial, 'passive' mixing process. The scaling of heat flux with the r.m.s. intensities no longer fully accounts for the decay of the heat transport, and the correlation coefficient, $\overline{w\theta}/w'\theta'$, decreases from its passive value.

This is the first indication in our data that the turbulence is a two-scale process in which the large scales are controlled by buoyancy forces and the small scales are dominated by dissipative processes. The preceding arguments are confirmed below by cross-spectral measurements of transport as a function of flow scale. An important corollary to this model of the collapse of the turbulent transport is that a zero net transport need not imply the absence of active mixing in the flow. Rather, it may imply only that the transport at large and small scales is equal and opposite.

For the highest values of t/τ, the heat flux correlation coefficient begins to increase again. This 'ringing' phenomenon may be the result of an increase in the vertical kinetic energy which is produced by a recovery of previously stored potential energy when the flow restratifies. One may speculate that such a ringing could persist, up and down, until all kinetic energy converted to potential energy was dissipated by the molecular destruction of scalar variance.

For future reference, we refer to the function described by the data in figure 2 as $f(t/\tau)$:

$$\overline{w\theta} = -w'\theta' f(t/\tau). \tag{11}$$

2.2. *Balance equation for vertical transport*

To further explore the mechanism by which buoyancy degrades the vertical convective heat flux, we consider the balance equation. In steady, stratified, transversely homogeneous (in y and z) turbulent flow, the evolution of $\overline{w\theta}$ is described by

$$U\frac{\partial}{\partial x}(\overline{w\theta}) = -\overline{w^2}\frac{\partial T}{\partial z} + \frac{g\overline{\theta^2}}{T} - \frac{1}{\bar{\rho}}\overline{\theta\frac{\partial p}{\partial z}} - (\nu+\alpha)\overline{\left(\frac{\partial\theta}{\partial x_j}\frac{\partial w}{\partial x_j}\right)}, \tag{12}$$

which neglects some higher-order terms that should be small. The terms on the right-hand side of this equation are, respectively, the production of heat flux by vertical turbulent mixing, the destruction of heat flux by the buoyancy forces which oppose scalar variance, the destruction of heat flux by the tendency to return to isotropy, and the destruction of heat flux by molecular dissipation. We have direct measurements of the first two right-hand-side terms.

Sirivat & Warhaft (1983) remark that the dissipative term ought to be negligible for moderately high Reynolds number in passively stratified flow. That conclusion is also likely to apply to the present flows. Non-zero dissipation requires correlation of w and θ at the small scales of motion, and the isotropy of those scales in the present flows leads to the vanishing of the cross-spectrum of $\overline{w\theta}$ at the same small scales which contribute, for example, to the dissipation of $\overline{u^2}$ and $\overline{\theta^2}$ (see §5.1). Hence, we shall assume the molecular dissipation of $\overline{w\theta}$ to be unimportant.

Now, the heat flux is generally carried by the larger scales of the flow, while dissipation acts only at the small scales of the flow (measurements of these scale

ranges are shown in §§3, 4, and 5). Turbulent pressure fluctuations have a spectral distribution similar to the distribution of $u^2(p \sim \frac{1}{2}\rho u'^2)$; thus, one might suppose that the correlation of temperature and pressure gradient, since it involves one derivative, will act on an intermediate range of scales.† The turbulent production and buoyant destruction terms, like the heat flux, are active at the large scales of the flow. Therefore, it seems of greatest interest to compare the turbulent production term to the buoyant destruction term, in order to gauge how well the overturning motions in the flow can compete with buoyant restratification effects in maintaining the turbulent convective heat flux.

The ratio of the production and buoyant destruction terms is

$$\frac{\overline{w^2}(\mathrm{d}T/\mathrm{d}z)}{g\overline{\theta^2}/T} = \frac{\overline{w^2}(\mathrm{d}T/\mathrm{d}z)^2}{\overline{\theta^2}N^2} = \left(\frac{L_\mathrm{b}}{L_\mathrm{t}}\right)^2 \tag{13}$$

This ratio is shown in figure 3 as a function of the buoyancy-scaled non-dimensional time. This figure has several points of interest. The first is that the ratio is simply a function of the non-dimensional time. A simple explanation for that is that the development of θ' is dependent upon the development of w', so that the ratio of these terms reflects only the accrued effect of buoyancy on the structure of the vertical stirring of the flow. Hence, the ratio can depend only on the buoyancy time and not on Re_λ, M, etc.

The second important feature is that the turbulent production of heat flux far exceeds the buoyant destruction in the 'passive' region of the flow. Studies of the passive case (Srivat & Warhaft) suggest that in this region the turbulent production and return-to-isotropy terms are approximately in balance, with the latter dominating somewhat. Conversely, in the region where the heat flux collapses, the production and destruction terms are essentially equal. One way to interpret this is that the collapse of the heat flux results from the lack of any net production with which to balance losses caused by the return-to-isotropy term.

An alternative interpretation of the ratio of production to destruction terms is possible. Suppose that we consider the ratio of an inertial timescale – one associated with overturning – to a buoyancy timescale. A simple choice for the overturning timescale would be $\tau_\mathrm{o} = L_\mathrm{t}/w'$, the time required for a particle travelling at the r.m.s. vertical velocity to travel the r.m.s. vertical displacement. A simple choice for the buoyancy timescale would be $\tau_\mathrm{b} = 1/N$.‡ The squared ratio of these is a Richardson number for overturning, Ri_o, and compares buoyancy forces to inertial forces at a given lengthscale:

$$Ri_\mathrm{o} \equiv \left(\frac{\tau_\mathrm{o}}{\tau_\mathrm{b}}\right)^2 = \left(\frac{NL_\mathrm{t}}{w'}\right)^2 = \left(\frac{L_\mathrm{t}}{L_\mathrm{b}}\right)^2. \tag{14}$$

Having identified the ratio in this manner, a new interpretation of figure 3 becomes possible. When the turbulent overturning motions are on a much smaller timescale than the buoyancy timescale, $Ri_\mathrm{o} \ll 1$, they are relatively unaffected by buoyancy

† The question of turbulent pressure spectra is more complicated than this simple argument implies. Discussion of the theoretical and experimental issues may be found in Batchelor (1953, §8.3) and George, Beuther & Arndt (1984). More detailed theoretical considerations do show, however, that $\overline{p^2}/\rho^2$ is determined principally by the range of wavenumbers near the peak of the velocity spectrum.

‡ We could equally well construct this estimate using the Väisälä period, $2\pi/N$. An identical result is obtained if the inertial timescale is replaced with the time required to travel a circle of circumference $2\pi L_\mathrm{t}$ (of radius L_t) at a speed of w'. Models which put turbulent particles on circular orbits are, however, somewhat unsettling.

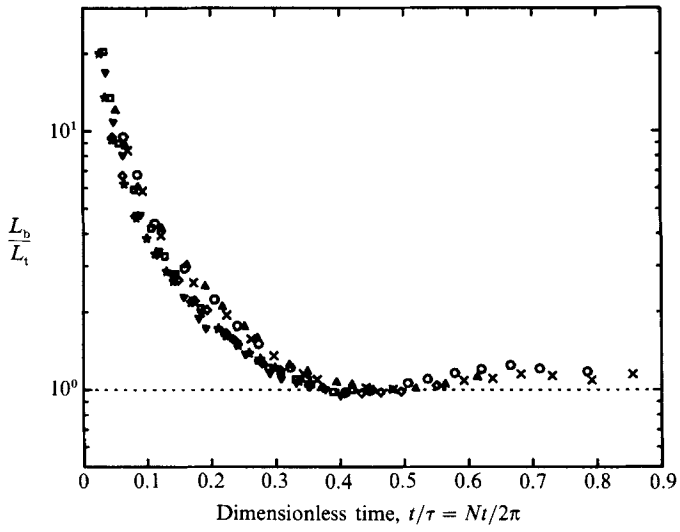

FIGURE 3. The ratio of heat flux production to destruction. $M = 5.08$ cm: ○, $N = 2.42\ s^{-1}$; △, $N = 2.17\ s^{-1}$; □, $N = 1.49\ s^{-1}$; ★, $N = 1.16\ s^{-1}$. $M = 2.54$ cm: ×, $N = 2.52\ s^{-1}$; ◇, $N = 2.17\ s^{-1}$; ▽, $N = 1.60\ s^{-1}$.

forces. The vertical transport of heat proceeds without interference, and the turbulent production of $\overline{w\theta}$ far exceeds the buoyant destruction. When the overturning and buoyancy timescales are of the same order, $Ri_0 \approx 1$, the turbulence is strongly influenced by buoyancy and the vertical transport of heat is retarded.†

2.3. *Streamwise convective heat flux*

The streamwise heat flux has had a rather chequered history in past studies and has frequently been ignored in studies of 'homogeneous' turbulent transport. We may use the present data to test certain expected features of $\overline{u\theta}$.

Tavoularis & Corrsin (1981) have argued that in turbulent flow such as the present one, energy conservation requires that $\overline{u\theta}$ is approximately constant in x when there is no streamwise temperature gradient. If the flow has true isotropy in x and y (axisymmetry about the z-axis), the correlation will be zero. In reality, the constant is non-zero and is determined by the initial conditions of the flow, since grid turbulence is always slightly anisotropic. Nevertheless, this correlation should retain its initial value. The associated correlation coefficient, $\overline{u\theta}/u'\theta'$, probably grows downstream, since u' decays faster than θ' grows.

The downstream evolution of $\overline{u\theta}$ and $\overline{u\theta}/u'\theta'$ is shown in figure 4(a, b) for the present data. The basic trend observed in the streamwise heat flux is a small region of initial development, during which the initial structure of the turbulent flow is still being established, followed by a lengthy region in which the heat flux is more or less constant, in agreement with the prediction. As suggested above, the non-zero flux may be the result of the initial conditions, perhaps associated with the slight anisotropy of the large eddies of the flow field. The final decay of the heat flux for the more heavily stratified runs is undoubtedly a result of the suppression of θ' by buoyancy forces.

† We note that L_b/L_t may be thought of as an overturning Froude number.

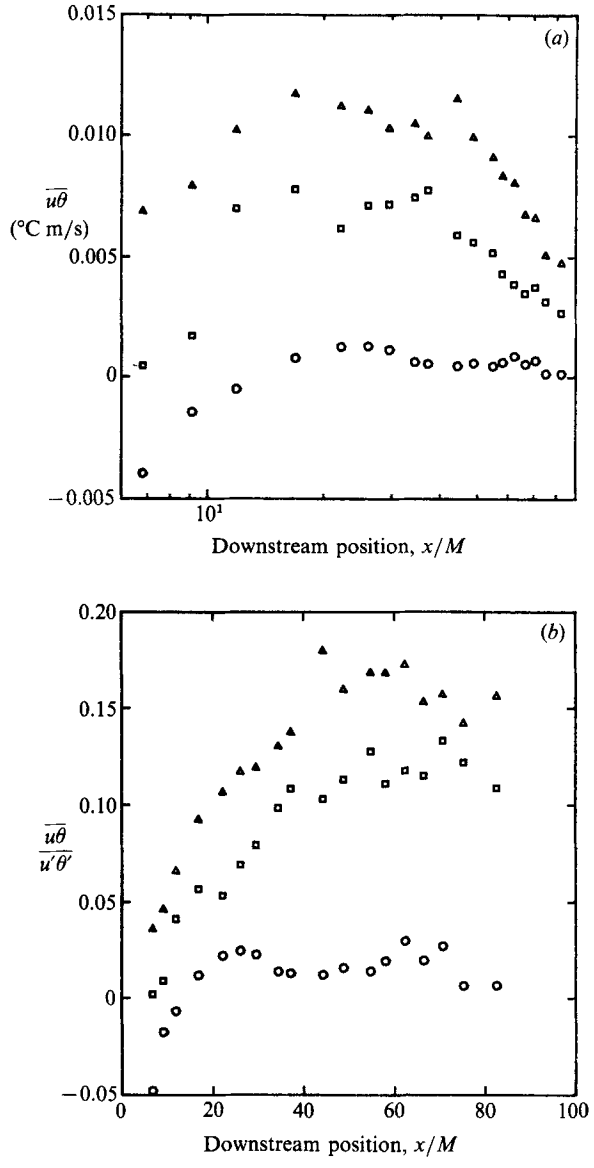

FIGURE 4. (*a*) The streamwise heat flux; (*b*) The streamwise heat flux correlation coefficient. $M = 5.08$ cm: ○, $N = 1.49$ s^{-1}; △, $N = 2.17$ s^{-1}; □, $N = 2.42$ s^{-1}.

The evolution of $\overline{u\theta}$ is governed by

$$U\frac{\partial}{\partial x}(\overline{u\theta}) = \frac{1}{\bar{\rho}}\overline{\theta\frac{\partial p}{\partial x}} + (\nu+\alpha)\left(\overline{\frac{\partial\theta}{\partial x_j}\frac{\partial u}{\partial x_j}}\right) \tag{15}$$

with $\partial T/\partial x = 0$. This equation seems to include no source term. The dissipation term, as for $\overline{w\theta}$, might be assumed to be relatively small.

How effective is the return-to-isotropy term in destroying the streamwise heat flux? This return-to-isotropy term cannot be very strong in the flow, since the decay of the streamwise flux is not very significant until the region of buoyancy influence is reached. This suggests that there is little correlation of θ and $\partial p/\partial x$, which,

perhaps, is not a surprising conclusion. The temperature fluctuations in the flow are most strongly associated with the vertical velocity fluctuations, and these might not play a large role in generating $\partial p/\partial x$. Pressure itself is a directionless quantity, but one may reason that horizontal velocity fluctuations would be most closely linked with horizontal pressure gradients. An analogous argument suggests an important role for the return-to-isotropy term in the vertical flux equation, in accord with our observations above.

Figure 4(*b*) shows that $\overline{u\theta}/u'\theta'$ increases steadily as one moves downstream (except for the run $N = 1.49\ s^{-1}$, $M = 5.08$ cm, which had a nearly zero flux). The growth slows once buoyancy effects become significant, a behaviour generally consistent with previous considerations. Other investigators studying non-isothermal grid turbulence have found, variously, that they obtained similarly large values of the correlation coefficient (-0.14, Yeh & Van Atta 1973) or that the correlation coefficient was smaller (0.065–0.096, Venkataramani & Chevray 1978). Most investigations of turbulent transport shy away from any discussion of this statistic, perhaps because of the theoretical notion that, in a fully isotropic turbulence, it must be zero.

3. Turbulent kinetic energies

In this section, we examine the influence of buoyancy on the development of the turbulent velocity field. The velocity evolution is much more well defined here than in previous salt-stratified water experiments, and several new features are uncovered. Moreover, the two-scale model of the turbulence, separating viscous and buoyancy effects, provides an excellent representation of this behaviour.

3.1. *Downstream development of* u′ *and* w′

Measurements of the vertical and streamwise components of the turbulent kinetic energy are presented as $(U/u')^2$ and $(U/w')^2$ in figures 5 and 6 for the 5.08 cm grid and various stratifications as a function of the non-dimensional distance from the grid, x/M. In the isothermal case, repeated investigation has shown that a power law of decay is followed during the 'initial period' of decay:

$$\left(\frac{U}{u'}\right)^2 = A\left(\frac{x}{M} - \frac{x_0}{M}\right)^n. \tag{16}$$

Such behaviour has also been observed in passively stratified non-isothermal flows (Montgomery 1974; Sreenivasan *et al.* 1980; Sirivat & Warhaft 1983). The exponents and virtual origins reported are typically in the ranges of $n = 1.2$–1.3 and $x_0 = 0 - 10$, respectively. We shall not use a virtual origin here, since the added complication does not materially assist us in reaching our objective.

The kinetic energy decay has several salient features. In the isothermal case, the two components u' and w' both decay at the same rate and follow a power law with an exponent of about 1.35. The initial level of isotropy at all stratifications is $w'/u' \approx 0.90$, a value similar to that found in other grid turbulence experiments (cf. Venkataramani & Chevray 1978).

The streamwise intensity shows no consistent effects of varying stratification. (The slight deviation for $N = 2.42\ \mathrm{s}^{-1}$ does not appear to be significant.) Conversely, the decay of w' is strongly accelerated by increasing the value of N. As discussed in detail by Itsweire *et al.* (1986), similar behaviour was observed by them and Lin &

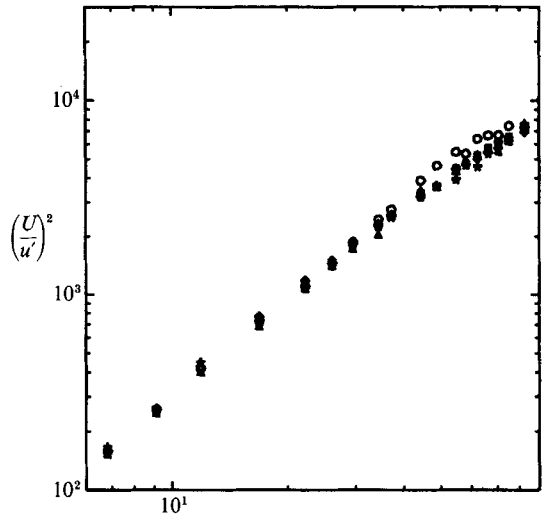

FIGURE 5.Decay of streamwise kinetic energy, $M = 5.08$ cm: ○, $N = 2.42$ s^{-1}; △, $N = 2.17$ s^{-1}; □, $N = 1.49$ s^{-1}; ★, $N = 1.16$ s^{-1}; ◇, $N = 0$ s^{-1}.

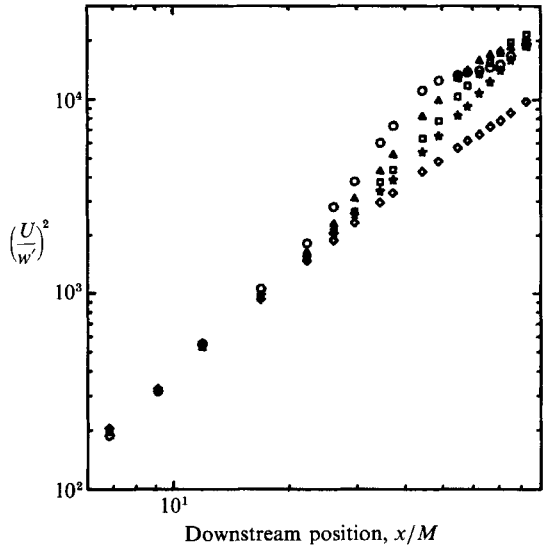

FIGURE 6. Decay of vertical kinetic energy, $M = 5.08$ cm: ○, $N = 2.42$ s^{-1}; △, $N = 2.17$ s^{-1}; □, $N = 1.49$ s^{-1}; ★, $N = 1.16$ s^{-1}; ◇, $N = 0$ s^{-1}.

Veenhuizen (1975) but not by Britter *et al.* (1983). That buoyancy effects are focused directly on w' is not unexpected since buoyancy retards vertical and not horizontal motions. That this effect is not carried over to u' is somewhat surprising and will be discussed when we consider the balance equations for $\overline{u^2}$ and $\overline{w^2}$ below.

These measurements of w' and u' are radically different from those obtained in previous actively stratified experiments in that the previous data, which were taken in salt water, were strongly influenced by internal waves and presented no well-defined pattern or inherent scaling behaviour. As we now elaborate, the present data are of a universal form.

3.1.1. *Universal scaling of vertical kinetic energy decay*

In figure 6, the general shape of the w' decay curve is the same for each stratification. The accelerated decay starts at some point, then levels out, and finally steepens again to parallel the isothermal curve. Prior to the visible onset of buoyancy effects, the curves are coincident for each stratification. These observations suggest that the decay of kinetic energy depends on two separate processes: the small-scale viscous decay phenomenon of grid turbulence and the suppression of large-scale vertical motion by Archimedean forces. Again, we see the two-scale nature of stratified grid turbulence.

We may construct a single decay curve for all stratifications by developing a scaling that separates the basic viscous decay from the accelerated decay produced by buoyancy forces. The integrated effects of buoyancy may then be represented with the dimensionless time, t/τ.

Since both u' and w' are affected by the viscous decay but u' is unaffected by buoyancy, we conclude that the viscous dissipation is relatively insensitive to stratification effects. This is concordant with the arguments of the preceding section and will be justified with direct measurements of ϵ below. Since the viscous and buoyant degradation of w' are essentially independent processes occurring at opposite ends of the spectrum, it is possible to view the accelerated decay of w' in terms of a deficit in w' produced by the accumulated influence of stratification.

This deficit might be characterized as the difference between w' at $N = 0$ and w' at a given stratification, and would still depend upon the elapsed time of viscous decay, that is, upon the distance of the point in question from the grid. Alternatively, we could normalize the turbulence intensity at any point downstream of the grid with that which would occur at the same point if no stratification were present. Presumably, this ratio would be independent of the viscous decay time, since the accumulated effect of viscous decay is identical for the two values of w' in question. (Here viscous decay is implicitly taken to function as a multiplicative decay factor in the sense of equation (16).) Thus, if we set

$$I_{\mathrm{w}}\left(\frac{x}{M}, \frac{t}{\tau}\right) = \left(\frac{U}{w'}\right)^2 \tag{17}$$

and denote its value for $N = 0$ as I_{w_0}, then the ratio I_w/I_{w_0} should be a function of t/τ only:

$$\frac{I_w(x/M, t/\tau)}{I_{w_0}(x/M)} = g(t/\tau). \tag{18}$$

The function $g(t/\tau)$ was calculated for the present experimental data, using the results for both the 5.08 cm grids and 2.54 cm grids, as shown in figure 7. The collapse is very good, and covers different values of N, M, U, and the related parameter Re_λ. That the scaling absorbs all of these factors is to be expected, since equation (16) shows w' to vary (under viscous effects) as

$$\overline{w^2} \propto A^{-1}U^2\left(\frac{x}{M}\right)^{-n}. \tag{19}$$

Stratified data should be normalized with unstratified data having the same values of x, M, and A to obtain the correct t and initial scales. Any sensitivity of the constant A to changes in other flow parameters could be compensated by scaling both I_w and I_{w0} with their initial values, although we have not done so here.

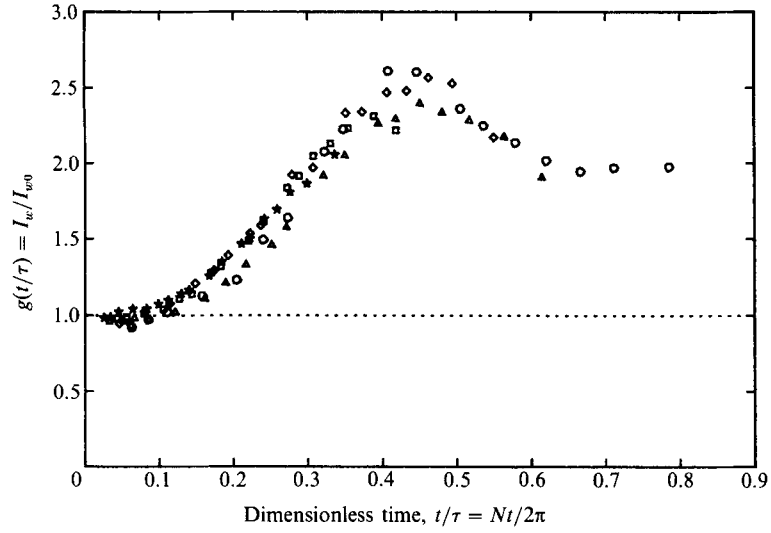

FIGURE 7. Universal decay of vertical kinetic energy. $M = 5.08$ cm: ○, $N = 2.42$ s^{-1}; △, $N = 2.17$ s^{-1}; □, $N = 1.49$ s^{-1}; ★, $N = 1.16$ s^{-1}. $M = 2.54$ cm: ◇, $N = 2.17$ s^{-1}.

The shape of this curve is easily interpreted in terms of the conversion of kinetic energy to potential energy. In the initial region of passive behaviour ($t/\tau < 0.1$) no buoyant suppression of the vertical kinetic energy occurs. The vertical dispersion of fluid particles grows downstream, increasing their potential energy with respect to the density gradient. The energy to support this increase can come only from the vertical kinetic energy of the fluid motion, which thus decays at a rate faster than that caused by viscous influence alone. Hence, $g(t/\tau)$ must increase. In this region ($0.1 < t/\tau < 0.3$), the vertical dispersion of fluid particles increases at the expense of their kinetic energy.

Beyond $t/\tau = 0.35$, the vertical motions of the turbulence have insufficient energy to sustain the vertically scattered state of the fluid particles, and buoyancy forces begin to drive them back toward their positions of buoyant equilibrium at a greater rate than they are dispersed by vertical stirring. During this restratification, some of the stored potential energy of these particles is recovered as kinetic energy (the remainder being lost to scalar dissipation) and $g(t/\tau)$ decreases again. The data beyond the region of restratification (which is roughly $0.35 < t/\tau < 0.60$) are limited. It appears that for $t/\tau > 0.6$, the vertical kinetic energy again decays at the unstratified rate, but at a level having about twice the value of $(U/w')^2$.

3.2. *The viscous dissipation rate*

The viscous dissipation rate, ϵ, was calculated by integration of the one-dimensional spectra for several different stratifications and mean speeds with the 5.08 cm grid. Dissipation spectra extended two decades below the peak of the dissipation spectrum for all cases; thus, the viscous dissipation is well resolved at even the first station, since most of the contribution to ϵ comes from the region near the peak. High-frequency noise in the dissipation spectra was removed by filtering prior to the integration for ϵ. Here, we investigate the possible effects of buoyancy on ϵ.

To account for the dependence of the dissipation rate upon the mesh size and mean speed, we use a simple scaling based on the assumption that the flow is isotropic. We make this assumption only to find the proper scaling behaviour. The degree to which

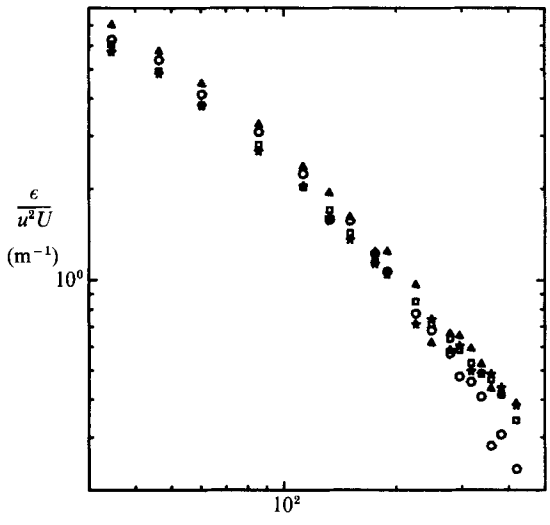

FIGURE 8. Isotropically normalized dissipation rate, $M = 5.08$ cm: ○, $N = 2.42$ s^{-1}; △, $N = 2.17$ s^{-1}; □, $N = 1.49$ s^{-1}; ★, $N = 1.16$ s^{-1}.

the actual anisotropy affects ϵ is discussed later in this subsection and in §3.4. The experimental values of ϵ were calculated using the quasi-isotropic form of Stillinger *et al.* (1983*b*): $\epsilon = \nu[10\overline{(\partial u/\partial x)^2} + \frac{5}{2}\overline{(\partial w/\partial x)^2}]$. We now use the definition (Batchelor 1953): $\epsilon = -3(\mathrm{d}/\mathrm{d}t)(\frac{1}{2}\overline{u^2})$. With (16) and Taylor's hypothesis ϵ may be written as

$$\frac{\epsilon}{\overline{u^2}U} = \frac{3n}{2}(x - x_0)^{-1}. \tag{20}$$

This normalized dissipation rate is independent of mesh size, mean speed, and initial conditions.

Equation (20) is used to represent the dissipation rate in figure 8. The normalized data collapse to within a scatter of about $\pm 15\%$ over the length of the test-section and for all stratifications. In the early portion of the tunnel, the curve has the predicted slope of -1, but the slope increases near the end of the tunnel to a value closer to -1.3. The increase in slope is most pronounced for the higher stratifications.

Since we have already found that u' is not significantly affected by buoyancy, nothing in the scaling offsets any effects of stratification. Thus, while figure 8 shows that ϵ is not strongly affected by the level of stratification, in agreement with our previous inferences, the increasing slope suggests that this is not the whole story.

To examine the possible influence of buoyancy more closely, let us directly compare the normalized dissipation rates to the unstratified dissipation rate and let us also take account of the scatter in the initial values of the scaled dissipation rate. Define

$$\epsilon^* = \frac{\epsilon/\overline{u^2}U}{(\epsilon/\overline{u^2}U)|_{N=0}} \tag{21}$$

and consider the ratio

$$\epsilon^*/\epsilon^*_{\mathrm{A}}, \tag{22}$$

where ϵ^*_{A} denotes the value of ϵ^* at station A. This ratio is plotted against the buoyancy coordinate, t/τ, in figure 9.

The resulting data are quite scattered, but the ratio in question is an error

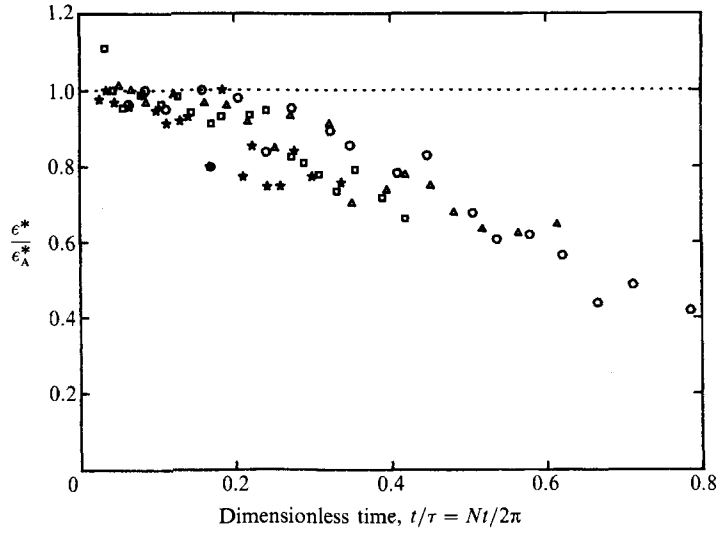

FIGURE 9. Buoyancy-scaled dissipation rate, $M = 5.08$ cm: ○, $N = 2.42$ s^{-1}; △, $N = 2.17$ s^{-1}; □, $N = 1.49$ s^{-1}; ★, $N = 1.16$ s^{-1}.

amplifier: each point involves the products and quotients of twelve measured quantities. Nonetheless, we have uncovered a distinct, if weak, buoyancy effect. Up to $t/\tau = 0.30$, all dissipation rates are within about 20% of the unstratified value. For larger values of t/τ, the dissipation rate begins to decline from its unstratified value, finally becoming 60% lower at $t/\tau = 0.8$. This behaviour was not uncovered in the previous salt-water experiments.

The pattern of reduction in ϵ is reasonable. As buoyancy time increases, the range of scales which suffer buoyancy effects includes increasingly small scales and eventually must encounter the small scales responsible for dissipation processes. The result is a breakdown of our two-scale model of the turbulence structure at large values of t/τ. The bulk of our data, however, is for buoyancy times small enough that the two-scale model remains a valuable conceptual tool.

3.3. *Kinetic energy balance equations*

To explore the transfer of buoyancy effects from the vertical to the horizontal velocity components, we consider the kinetic energy balance equations for a steady, anisotropic, turbulent flow which is homogeneous in y and z. Without certain terms which are negligible (Lienhard 1988), the balance equations for $\overline{u^2}$ and $\overline{w^2}$ reduce to

$$U\frac{\partial}{\partial x}(\tfrac{1}{2}\overline{u^2}) = \frac{1}{\bar{\rho}}\overline{p\frac{\partial u}{\partial x}} - \nu\overline{\left(\frac{\partial u}{\partial x_j}\right)^2} \tag{23}$$

and

$$U\frac{\partial}{\partial x}(\tfrac{1}{2}\overline{w^2}) = \frac{1}{\bar{\rho}}\overline{p\frac{\partial w}{\partial z}} - \nu\overline{\left(\frac{\partial w}{\partial x_j}\right)^2} + \frac{g\overline{w\theta}}{T}. \tag{24}$$

The balance equation for the total kinetic energy, $q^2 = (u'^2 + v'^2 + w'^2)$, is

$$U\frac{\partial}{\partial x}(\tfrac{1}{2}q^2) = -\epsilon + \frac{g\overline{w\theta}}{T}. \tag{25}$$

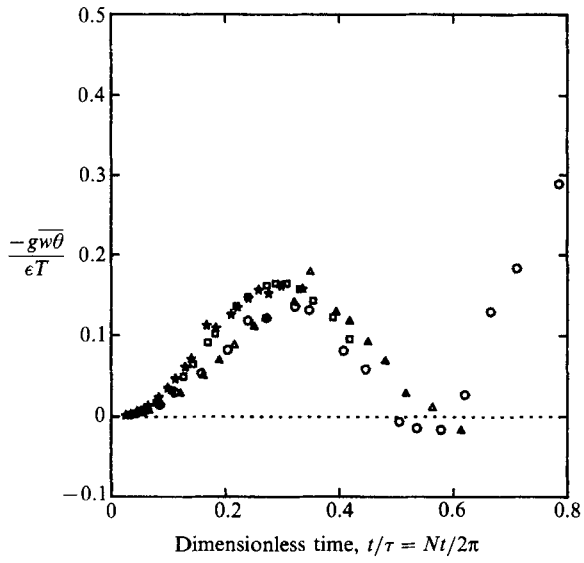

FIGURE 10. Ratio of kinetic energy sinks, $M = 5.08$ cm: ○, $N = 2.42$ s^{-1}; △, $N = 2.17$ s^{-1}; □, $N = 1.49$ s^{-1}; ★, $N = 1.16$ s^{-1}.

Consider first the overall kinetic energy balance. We may quantify the effect of the buoyancy work term on the total kinetic energy by considering the ratio of it to the viscous dissipation term, as is done in figure 10 for several stratifications. The figure shows the apparent collapse of these curves under a buoyancy scaling, which is somewhat surprising given that the buoyancy and dissipation processes are independent; the cause may be that ϵ characterizes the magnitude of the local overturning processes which contribute to $\overline{w\theta}$.

The buoyancy work term is generally not large compared with the viscous dissipation. For small buoyancy times (passively stratification), the buoyancy work is negligible. The ratio subsequently grows to about 0.16 and then decays toward zero again, mirroring the basic trends of particle dispersion previously discussed. Particles migrating farther from their equilibrium locations experience increasing buoyancy forces; as their vertical dispersion is suppressed and reversed by buoyancy forces (and as molecular dissipation consumes scalar variance), the magnitude of the buoyancy work decreases. For a small region of the flow, the buoyancy work is actually positive: the restratification of the flow leads to some recovery of the stored buoyant potential energy as kinetic energy.

For very large values of the buoyancy time, the ratio increases sharply, probably signalling the presence of active buoyancy forces at all scales of the motion. The large and small eddies are no longer so different that dissipative processes are unaffected by buoyancy forces, as evidenced by the buoyancy scaling of ϵ above.

Throughout most of the flow, buoyancy work plays a rather small role in the decay of the total kinetic energy, amounting to local losses of less than 16% for $t/\tau < 0.6$. We have seen, however, that its effects on the vertical kinetic energy are more significant, amounting to as much as a 50% decrease in $\overline{w^2}$. Since $\overline{w^2}$ is roughly one-third of q^2, this suggests that the decrease seen in q^2 should not exceed one-sixth, or about 16%, of its total value. Indeed, that appears to be the case. Thus, the decrease in the total kinetic energy (from the $N = 0$ case) is wholly associated with a decrease

in w'; the measurements of u', w', and the sinks of total kinetic energy are in accord on this point.

The observation is not surprising when one considers that the buoyancy work term enters the total kinetic balance through its appearance in the balance equation (24) for $\overline{w^2}$. What is surprising is that the pressure–velocity gradient correlations – the return-to-isotropy terms – do not appear to transfer the accelerated decay of w' to the other velocity components. The small transfer of energy from the horizontal components of velocity to the vertical component signals only a minor role for the return-to-isotropy terms.

The small effect of the vertical kinetic energy decay on the decay of total energy may also be the reason for the relative insensitivity of the viscous dissipation rate to buoyancy influences for buoyancy times less than $t/\tau \approx 0.4$.

3.4. *Universal equilibrium spectra*

The viability of Kolmogorov universal equilibrium scaling in a stratified environment has been questioned on the grounds that buoyant suppression of active mixing ultimately alters the energy cascade. Gibson (1980) proposed that the increasingly strong influence of buoyancy forces would render Kolmogorov scaling irrelevant as the turbulence becomes fossilized. Experimental tests of this proposition have been difficult in salt-water flows (Stillinger *et al.* 1983*b*; Itsweire *et al.* 1986), and it is thus worthwhile to undertake such scalings here.

For $N = 0$, figure 11*a* shows the universal scaling of the vertical turbulent intensity spectra at all streamwise stations except G and J for a mesh of 5.08 cm. Universal equilibrium scaling collapses the high-frequency portion of all sixteen spectra to a single curve. The low frequencies also collapse to a large extent for stations beyond $x/M = 20$. For stations with $x/M < 20$, (the four highest curves, stations A**–C), the flow is still adjusting to its passage through the grid (particularly at the largest scales) and is not as homogeneous; at these four stations neither the low nor the high frequencies of the spectrum conform well to the universal curve. However, for the remaining stations, the universal scalings give excellent results for the isothermal case.

The next test of universal scaling is to apply it to various spectra for a single non-zero stratification. Figure 11(*b*) shows the universally scaled spectra of the vertical turbulent velocity for $N = 2.42$ s^{-1} and all downstream stations except D, E′, and J′. The collapse of the high-frequency ends of the fifteen curves is excellent, indicating that scaling is effective for any given stratification. (Similar results were obtained for other stratifications.) The low-frequency ends of the curves initially decay strongly, and then rise again as the large scales restratify. Both the high and low wavenumbers collapse to a single curve for stations beyond $x/M = 20$. (The near-grid stations are again the four high curves at low wavenumbers and the four low curves at high wavenumbers.) Universal equilibrium theory works very well at the high wavenumbers in spite of the very strong effects of buoyancy.

Perhaps the most important test of universality is whether the spectra for different stratifications are similar to one another. This collapse was made for stratifications of $N = 0$, 1.49, 2.42 s^{-1} using data from stations F′, H′,and J. (The $N = 0$ spectra do not include station J.) The results are shown in figure 11(*c*) for E_{ww}. The spectra conform very well to universal equilibrium scaling, with an error of about $\pm 10\%$ for $\kappa\eta = 0.5$.†

† The sharp spectral roll-off in this range exaggerates the ordinal error for a fixed abscissa.

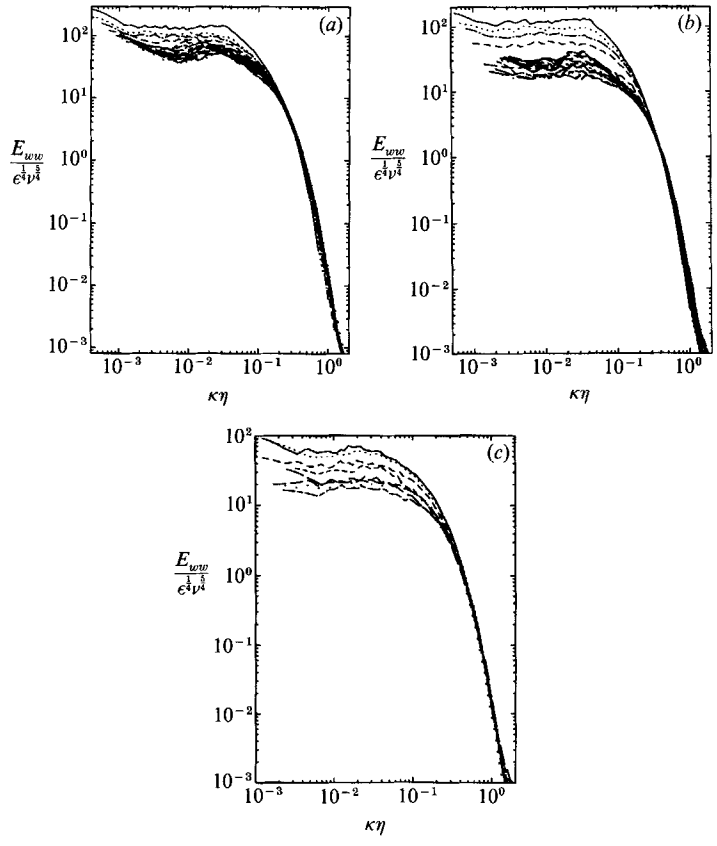

FIGURE 11. Universal scaling of E_{ww} for $M = 5.08$ cm: (*a*) $N = 0$: —, A**; ···, A; –·–, B; – – –, C; (*b*) $N = 2.42$ s^{-1} (labels as for *a*); (*c*) $N = 0$ s^{-1}: —, F′; ···, H′. $N = 1.49$ s^{-1}: – – –, F′; ———, H′; – – –, J. $N = 2.42$ s^{-1}: ···, F′; ——, H′; – – –, J.

The low frequencies of the E_{ww} spectra are of interest. The spectra for upstream stations are above those for downstream stations and those for lower stratifications are generally higher than those for heavier stratification, owing to buoyant suppression of w. An important exception occurs for E_{ww} at the heaviest stratification, where the low-frequency ends of the curves grow downstream and exceed those for the intermediate stratification at some downstream stations. This is the result of restratification, which adds energy to the low-frequency portion of the spectrum. The high-frequency collapse is somewhat better for E_{ww} than for E_{uu}, which is not shown.

We conclude that universal equilibrium scaling gives excellent results in stratified turbulence up to buoyancy times as large as $t/\tau = 0.70$. Some deviation occurs in the near-grid region, but this is primarily attributable to the rapidly changing structure of the large scales.

4. Development of the scalar field

4.1. *Temperature variance*

The magnitude of the temperature fluctuations is dependent upon the initial disturbance set by the grid, the mean temperature gradient (which characterizes

the variance produced by an overturn of a given size), and the distance from the grid. The streamwise evolution of the scaled r.m.s. temperature fluctuation, $L_t = \theta'/(\mathrm{d}T/\mathrm{d}z)$, was measured for both grids at several stratifications and was found to be of the same general shape for both grids.

The curves for the two grid sizes appear only to be displaced by an initial scale factor, a result of the larger overturning motions produced by the big grid. An exception occurs for the larger grid with $N = 1.16\ \mathrm{s}^{-1}$. At this small stratification, the grid does not generate sufficiently large temperature disturbances to fully eradicate the upstream noise (see discussion in Lienhard & Van Atta 1989); the initial L_t thus exceeds the true grid value. This run is excluded from the scaling which follows.

Since L_t is proportional to w', and w' is proportional to $M^{n/2}$ (for passive stratification, according to (16)), then L_t should also be proportional to $M^{n/2}$. Hence, the relationship between the data for the two grid sizes should be

$$L_{t|_{5.08}} = \left(\frac{5.08}{2.54}\right)^{n/2} L_{t|_{2.54}}. \tag{26}$$

Since $n \approx 1.35$ for our data (without a virtual origin, using stations away from the grid), the scale factor is about 1.60.

The two sets of data agree quite well after multiplying the $M = 2.54$ cm data by 1.60, but some empirical adjustment to the scale factor may be made in order to account for minor differences in the initial conditions and physical properties for various stratifications (namely, the constant A). Such adjustments amount to no more than 6%, and the final scaled data are shown in figure 12; the values of L_t shown collapse to within about $\pm 7\%$ in the passive stages of development.

Buoyancy has a definite influence on the downstream development of L_t. Initially, θ' grows at the same rate for all stratifications: a power-law growth roughly proportional to $x^{0.41}$. Father downstream, the scalar variance begins to decline. This decline occurs sooner and more strongly for the heavier stratifications. As elaborated below, the decrease results from the reduction in variance production by buoyant suppression of vertical particle migration and the subsequent dominance of the molecular dissipation of scalar variance.

Similar evolution of L_t was observed in salt-stratified water by Stillinger (1981) and subsequently by Itsweire *et al.* (1986). The transition from growth to decay of the scalar is sharper in salt water, which is indicative of the greater role of molecular dissipation in the air flow.

The relationship between L_t and w' is more fundamental than might be inferred from the preceding remarks. The reader may recall figure 3 which shows that the ratio L_t/L_b is a unique function of the dimensionless buoyancy time, t/τ. Thus, the development of the scalar variance is directly tied to the history of the vertical turbulence intensity. Figure 4 represents a complete scaling of θ'.

4.2. *Scalar dissipation rate*

The present experiments include direct measurements of the scalar dissipation rate, χ. Great care was taken to ensure that the temperature spectra were sufficiently well resolved to allow direct integration for χ. Typical dissipation spectra, which support this assertion, are presented below. The isotropic formula was used: $\chi = 6\alpha\overline{(\partial\theta/\partial x)^2}$. Evidence supporting the isotropy of the small scales is given in §§3.4, 4.4.1, and 5.3. The universality of the scalar spectra (below) militates for the accuracy of the values of χ so computed. Our ability to balance the scalar variance budget also supports

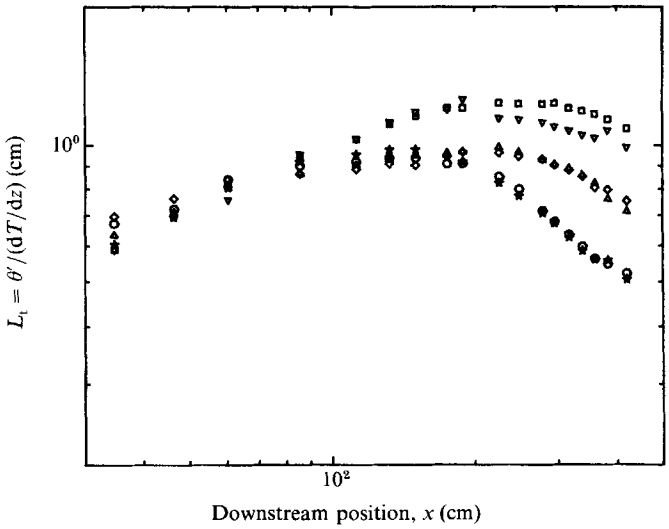

FIGURE 12. Overturning scale, L_t, small-grid-data scaled: $M = 5.08$ cm: ○, $N = 2.42$ s^{-1}; △, $N = 2.17$ s^{-1}; □, $N = 1.49$ s^{-1}. $M = 2.54$ cm: ★, $N = 2.51$ s^{-1} ($\times 1.50$); ◇, $N = 2.17$ s^{-1} ($\times 1.57$); ▽, $N = 1.60$ s^{-1} ($\times 1.68$).

these measurements. Instrument resolution is discussed at length by Lienhard (1988).

Scalar dissipation is driven by the large eddies of the flow. The 'energy' of temperature fluctuations is like θ'^2 and the timescale for transfer of such energy from the large eddies to the small eddies is like the timescale for vertical overturning, L_t/w'. Hence, the molecular dissipation rate in stratified turbulence should scale as

$$\chi \sim \frac{w'\theta'^2}{L_t}. \tag{27}$$

The magnitude of temperature fluctuations is proportional to the mean temperature gradient for a fixed velocity field. A logical normalization of the scalar dissipation rate then appears to be the Cox number:

$$Co = \frac{\chi}{2\alpha(dT/dz)^2}. \tag{28}$$

The Cox number has often appeared in the literature on oceanographic microstructure.

Apparently, the Cox number will be directly sensitive to the large-scale suppression of L_t, via the dependence of χ on θ'. While L_t plainly depends upon both w' and the buoyancy time, t/τ, a simple approach to the scaling of χ is simply to plot Co as a function of t/τ. Such a graph is presented in figure 13 for the 5.08 cm grid. The figure shows, in fact, that for buoyancy times greater than about 0.1, the Cox number is well represented as a function of t/τ alone. For the smaller times which represent passive stratification, the Cox number appears to depend on additional factors.

The dependence of Co on t/τ alone is somewhat unexpected, given the dependence of L_t on w' and the dependence of Co upon a quantity like $L_t w'$. It would seem that Co ought to depend upon the parameters that describe the turbulence evolution as

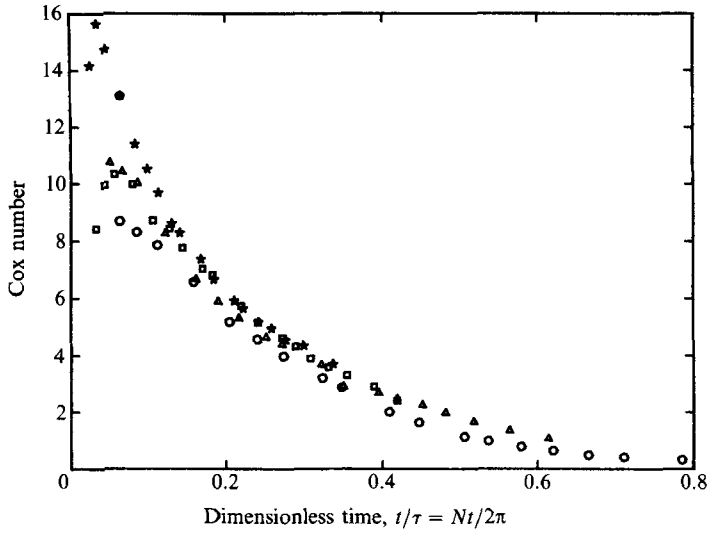

FIGURE 13. Buoyancy influence on the Cox number, $M = 5.08$ cm: ○. $N = 2.42$ s^{-1}; △, $N = 2.17$ s^{-1}; □, $N = 1.49$ s^{-1}; ★, $N = 1.16$ s^{-1}.

well. However, we may explain the observed behaviour by introducing a thermal microscale, λ_θ, following the (isotropic) definition of Corrsin (1951*b*):

$$\chi = 12\alpha \frac{\theta'^2}{\lambda_\theta^2}. \tag{29}$$

With this, the Cox number may be written as a ratio of the thermal overturning scale to the thermal microscale:

$$Co = 6\left(\frac{L_t}{\lambda_\theta}\right)^2. \tag{30}$$

The microscale does not represent the average size of the dissipative eddies, which is of order η_θ, the Corrsin scale. However, it does scale the dissipation of scalar variance against the r.m.s. temperature scale, θ'. Thus, we may still interpret the Cox number as a squared ratio of the overturning scale to one which characterizes the dissipative scales.

In this light, the dependence of the Cox number upon the buoyancy time alone (for active stratification) is less surprising. The buoyant degradation of the large scales of the flow drives the variance-producing scales towards the dissipative scales. In a passively stratified flow, this type of scale separation might be characterized by a microscale Reynolds number, and, in the present case, Re_λ is relatively constant away from the immediate vicinity of the grid. Thus, the scale separation represented by the Cox number is unaffected by the ordinary viscous decay of the turbulence, and it may thus be expected to be a function of buoyancy time alone. A corollary to this interpretation is that the uncorrelated variations of Co for small buoyancy times may be associated with the changes in Re_λ in that region.

4.2.1. *The role of dissipation in particle dispersion*

Generally, our remarks about the dispersion of fluid particles have been made with the simple-minded assumption that a particle has a distinct equilibrium position with respect to the temperature gradient. While this is true instantaneously, the

equilibrium level of any particle will change if its temperature changes. Thus, a primary effect of the molecular dissipation of heat is to assign new equilibrium levels to particles by changing their temperatures.

The effect is quite important in the present flow because the molecular destruction of scalar variance is of the same order as the turbulent production. Thus, the roll-off in L_t must be recognized to be significantly affected by the adjustment of displaced fluid particles to the temperature of their surroundings, as well as the reduction in variance production by the buoyant suppression of overturning motions. (The scale separation of molecular and restratification effects is further illustrated in §5.) Another important feature of the destruction of scalar variance by molecularity is that it represents an irreversible dissipation of the potential energy available for driving restratification processes.

4.3. *Scalar variance balance*

The development of temperature variance in a steady, vertically stratified flow of uniform mean velocity U, homogeneous in the (y, z)-plane, is described by the following equation (excluding certain negligible terms):

$$U\frac{\partial}{\partial x}\overline{\theta^2} = -2\overline{w\theta}\frac{\mathrm{d}T}{\mathrm{d}z} - \chi. \tag{31}$$

The first term on the right-hand side is the production of scalar variance by turbulent stirring of the flow. The second is the molecular dissipation of scalar variance. The relative strength of these terms determines whether or not the temperature variance will grow. The ratio of these terms is shown in figure 14 for the 5.08 cm grid.

The ratio has been presented as a function of t/τ, and this scaling seems to bring the curves close together. The appearance of a single curve may be rationalized by combining our scale estimate for χ, (27), with (11). Together, those results reveal that the ratio of scalar variance production to dissipation scales like

$$\frac{2\overline{w\theta}(\mathrm{d}T/\mathrm{d}z)}{\chi} \sim 2f(t/\tau), \tag{32}$$

which makes it a function of t/τ only. The figure shows that the production-to-destruction ratio has the same general form as the curve $f(t/\tau)$ shown in figure 2(*b*). The scale argument seems to fail in the passive region of the flow ($t/\tau < 0.1$), although this could be related to the proximity of the grid. The ratio ceases to behave like $f(t/\tau)$ for $t/\tau > 0.6$ where it grows sharply. In that region, the heat flux grows again as a result of 'restratification overshoot', but the scalar dissipation does not keep pace. This may signal the breakdown of the vertical overturn timescale as that appropriate to energy transfer from the variance-producing eddies to the dissipative eddies; the separation of those scales has at this point become fairly small.

The location at which the ratio equals one marks the transition from growth to decay of θ'. This location on the production/dissipation curve corresponds roughly to the points at which the L_t curves begin to decline.

4.4. *Temperature spectra*

Figure 15(*a*) shows temperature spectra in the passive region of one typical flow. The spectra show decay at the high frequencies, where molecular processes dominate. The spectra grow at large scales as a result of the vertical dispersion of particles which increases variance. Figure 15(*b*) shows temperature spectra in the same flow farther

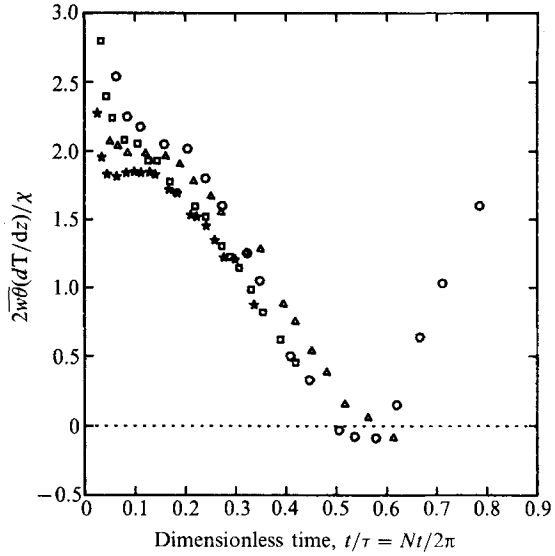

FIGURE 14. Production/dissipation of $\overline{\theta^2}$, $M = 5.08$ cm: ○, $N = 2.42$ s^{-1}; △, $N = 2.17$ s^{-1}; □, $N = 1.49$ s^{-1}; ★, $N = 1.16$ s^{-1}.

downstream (stations G′, G, H′, I′, I) where buoyancy effects have taken control of the large-scale behaviour. Here, the large-scale energy of the spectrum decreases steadily. The last curve shows growth at large scales; it lies in the restratifying region of the flow.

Figure 15(*c*) shows some typical scalar dissipation spectra. The remarks that apply to these spectra are identical to those made in regard to the viscous dissipation spectra in §3.2. Resolution of the scalar dissipation spectrum is quite adequate to provide accurate measurements of χ.

Typical spectral bandwidths are shown in figure 15(*d*) for the scalar variance, the vertical convective heat transport, and the scalar dissipation rate. The spectra are given in area-preserving form with arbitrary vertical amplitudes, and correspond to station C in the same flow. The figure shows that heat transport and scalar variance are dominated by the same range of large scales at this location.

4.4.1. *Universal equilibrium scaling*

An important issue which may now be addressed is the universal equilibrium scaling of the temperature spectrum. While universality of $E_{\theta\theta}$ has long been accepted by turbulence researchers in the passive case, it has recently been challenged by Gargett (1985) on the basis of her oceanographic measurements. Thus, we can pursue this question with a renewed vigour.

According to Obukhov (1949), Corrsin (1951*a*), and Batchelor (1959), the spectra should be given by a universal function, F_θ, when scaled as

$$F_\theta(\kappa\eta, Pr) = \frac{E_{\theta\theta}(\kappa\eta)}{\chi(\nu^5/\epsilon^3)^{\frac{1}{4}}}. \tag{33}$$

The temperature spectra were scaled in this fashion for $N = 2.42$ s^{-1} and $M = 5.08$ cm at fifteen streamwise stations (figure 16*a*). For high wavenumbers, the collapse of the spectra is excellent. As for the velocity spectrum, the lowest curve at high

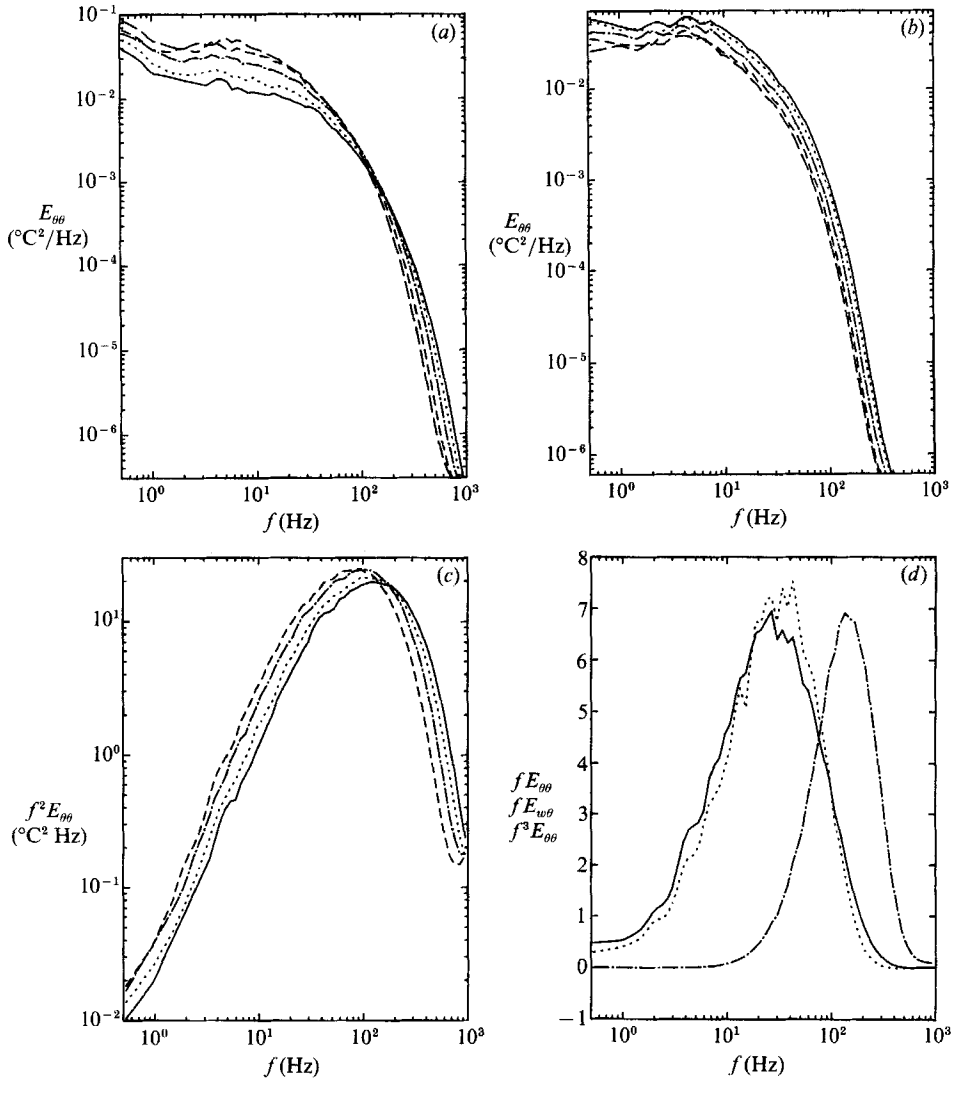

FIGURE 15. Various temperature spectra, $N = 2.42$ s^{-1} and $M = 5.08$ cm. (*a*) Passive temperature spectra: —, A**; ···, A; –·–, B; – – –, C; ————, D. (*b*) Active temperature spectra: —, G′; ···, G; –·–, H′; – – –, I′; ————, I. (*c*) Scalar dissipation spectra: —, A**; ···, A; –·–, B; – – –, C. (*d*) Bandwidths for scalar quantities, Station C (vertical scales arbitrary): —, $fE_{\theta\theta}$; ···, $fE_{w\theta}$; –·–, $f^3E_{\theta\theta}$.

wavenumbers is for the station nearest the grid, but even it is in good agreement with the universal spectrum. The same type of graph is shown for $N = 1.49$ s^{-1} and $M = 5.08$ cm in figure 16(*b*), with equally good results.

Scaled temperature spectra are shown in figure 17 for several stratifications and streamwise stations ($N = 2.42, 2.17, 1.49$ s^{-1}, $M = 5.08$ cm at stations F′, H′, and J; station H′ was omitted for $N = 2.17$ s^{-1}.) The spectral agreement is again excellent, with a vertical error of $\pm 15\%$ at $\kappa\eta = 0.5$ (exacerbated by the steep slope in this region). No differences are present in the high-wavenumber behaviour of the spectra for different N or streamwise locations for either passively or actively stratified regions of the flow.

The present data thus fully support the universal similarity of the scalar spectrum

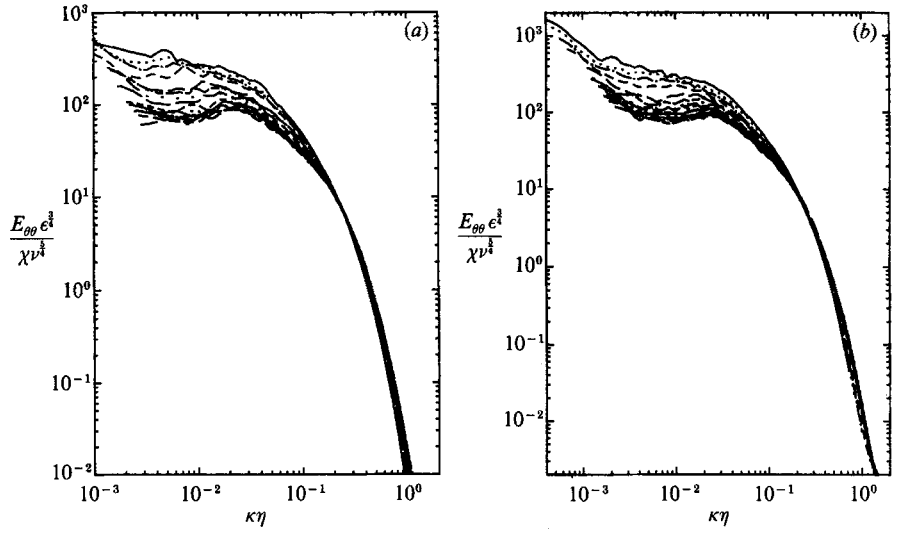

FIGURE 16. Universal equilibrium scaling of $E_{\theta\theta}$ for $M = 5.08$ cm with (*a*) $N = 2.42$ s^{-1} and (*b*) $N = 1.49$ s^{-1}: —, A**; ···, A; –·–, B; – – –, C.

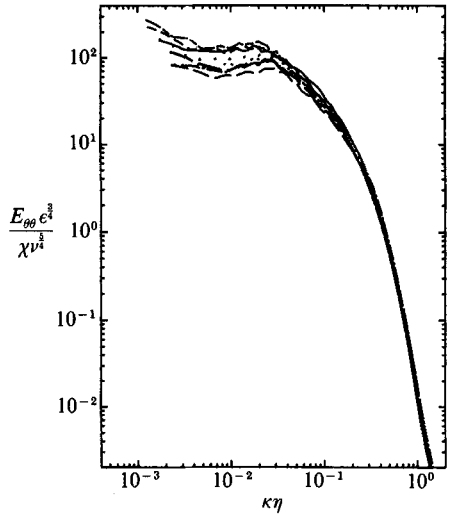

FIGURE 17. Universal equilibrium spectra for $E_{\theta\theta}$. $N = 2.42$ s^{-1}: —, F′; ···, H′; –·–, J. $N = 2.17$ s^{-1}: – – –, F′; ————, J. $N = 1.49$ s^{-1}: ——, F′; ···, H′; ————, J.

for large wavenumbers in the presence of buoyancy effects at small wavenumbers, but cannot resolve the peculiar inertial subrange behaviour observed by Gargett. Further controlled laboratory measurements at larger Reynolds number might shed more light on her results.

5. Cospectra, phase, and the low frequencies

In this section, we use the cospectrum and phase of $\overline{w\theta}$ to analyse the spectral distribution of the vertical convective heat transfer and thence to make direct inferences regarding the structure of stratified turbulence. These data enable further

differentiation of the ranges of scales associated with active stirring, restratification, and molecular mixing.

5.1. *Cospectral measurements*

Figure 18 (a, b) shows the cospectrum, $Co_{w\theta}$, in area-preserving form (multiplied by f) for one stratification and two different mesh sizes. The cospectra are not normalized and the relative vertical heights of the curves are directly proportional to the amount of vertical transport present at a given frequency. The peak of $Co_{w\theta}$ decreases steadily in the downstream direction. All of the cospectra decay steadily at high frequencies under the effects of molecular viscosity and conductivity. The high-frequency portions of these spectra all have a similar shape, and this similarity is shown to be of universal form in §5.2.

We have already seen that the bandwidths active in the vertical heat transport are roughly the same as those associated with the variance-producing eddies. An important difference between the cospectrum and the usual power spectrum, however, is that the cospectrum may change sign. A negative value of $Co_{w\theta}$ indicates the downward (cogradient) transport of heat, whereas a positive value indicates upward (countergradient) transport. The figures show $-Co_{w\theta}$, so that the portions of the curves which fall below zero on these graphs represent countergradient heat flux.

The low-frequency ends of the cospectra show no decay prior to the onset of buoyancy effects; they retain the same energy level as the high-frequency ends are being degraded by molecular effects. This behaviour may be interpreted as a kind of permanence of the large eddies. Figure 19 shows some of these passive cospectra alone. Once buoyancy effects set in, however, the large scales of the flow begin to collapse. Figure 18 (a, b), which extends to larger values of the buoyancy-scaled time, show not only the complete loss of the large-eddy transport, but also a change in the sign of the cospectum over a certain bandwidth: these frequencies are responsible for countergradient transport. Heat is carried from cold regions to hot regions.

The countergradient transport of heat is associated with only large scales of motion, as the selected curves of figure 20 (a) illustrate. This observation suggests that countergradient transport is the result of restratification: as the large eddies are crushed by buoyancy forces, fluid particles are moved toward their positions of buoyant equilibrium, resulting in the transport of hot eddies upward and of cold eddies downward. Of equal importance is the continuing presence of active vertical heat transport at the smaller scales while restratification occurs at the large scales. Thus, restratification need not produce a net downward flow of heat, merely a downward flow of heat on a limited range of scales. In order for $\overline{w\theta}$ itself to change sign, the area beneath a cospectral curve must change sign. This does happen for some cases, but, in general, restratification occurs even in the presence of net cogradient transport.

Evidently, $\overline{w\theta}$ may vanish even while active mixing continues at the small scales of the flow. It is therefore inappropriate to treat $\overline{w\theta} = 0$ as a sufficient criterion for the complete suppression of vertical transport, as has sometimes been done in the stratified-flow literature. We must note that the present data are for a much different Prandtl number than the salt-water experiments for which the criterion was developed (Stillinger 1983*b*; Itsweire *et al.* 1986) and that the theoretical predictions of Deissler (see below) show a strong Pr effect upon the cospectral collapse. Even so, accurate determination of the state of turbulence in a stratified flow requires measurements of the cross-spectrum, rather than just the cross-covariance.

We previously noted a 'ringing' effect in the vertical heat transport at large values of the buoyancy time, for which the vertical transport returns from zero or positive

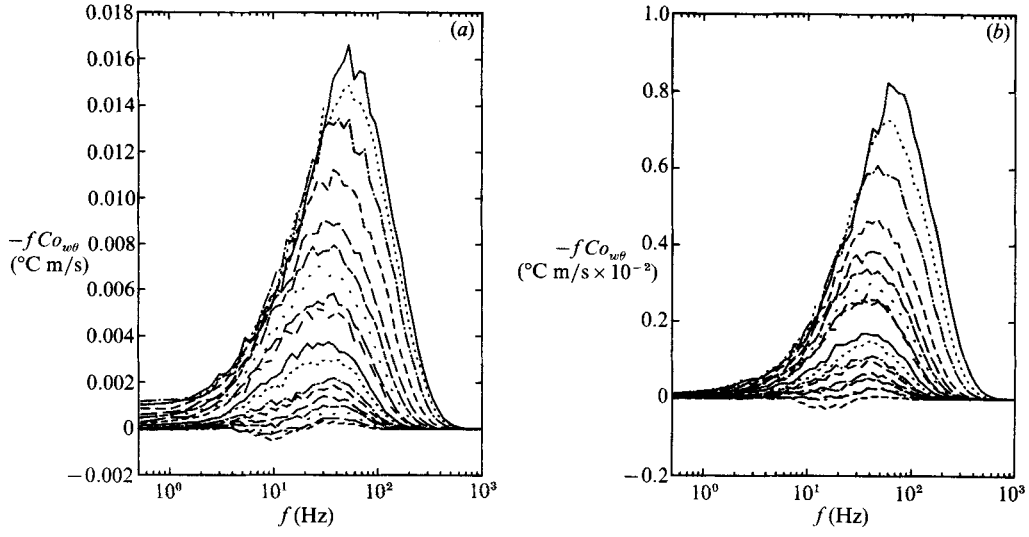

FIGURE 18. Cospectral development for $N = 2.17\ \mathrm{s}^{-1}$: (*a*) $M = 5.08$ cm; (*b*) $M = 2.54$ cm.

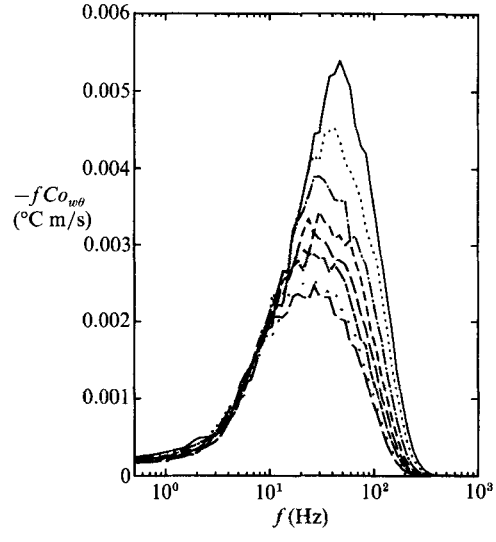

FIGURE 19. Passive cospectra for $N = 1.16\ \mathrm{s}^{-1}$ and $M = 5.08$ cm: stations A–F.

values to a state of net cogradient transport. In this region (figure 20*b*), the restratifying bandwidth decreases until all the area beneath the curve is again of one sign, and the large scales of the flow are again actively transporting heat. The restratification arrests. The reappearance of active transport at the large scales may be caused by an increase in the vertical kinetic energy resulting from the recovery of some of the stored potential energy.

5.2. *Universal similarity of the cross-spectrum*

It seems obvious that the universality of the velocity and temperature spectra ought to imply some kind of universality for the cross-spectrum. The high-wavenumber behaviour of the cospectrum also suggests such a similarity. The presence of such a

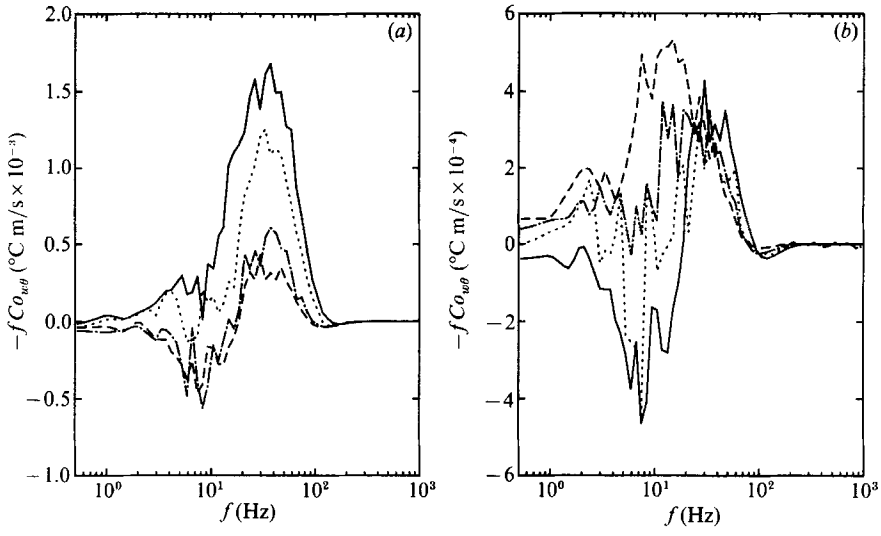

FIGURE 20. (*a*) Cospectral collapse: $N = 2.42\ \mathrm{s}^{-1}$ and $M = 5.08$ cm: –, G′; ···, G; –·–, H′; – – –, H; (*b*) cospectra for restratification overshoot, $N = 2.42\ \mathrm{s}^{-1}$ and $M = 5.08$ cm: —, H; ···, I; –·–, J′; – – –, K′.

similarity would be additional evidence of the independence of the small scales of the turbulence from the Archimedean forces which come to dominate the large scales.

To deduce such a similarity of the cospectrum, we could construct formal Kolmogorov-type arguments for the spectral transfer of $\overline{w\theta}$-stuff from the low wavenumbers to the high wavenumbers, arguing a balance of the input of $\overline{w\theta}$-stuff from the energy-containing wavenumbers and the molecular diffusivity of $\overline{w\theta}$-stuff at high wavenumbers. The difficulty with such an argument is, as noted in §2.2, that molecular dissipation of $\overline{w\theta}$ is probably not significant, since small-scale isotropy implies the vanishing of $E_{w\theta}$ at high wavenumbers. Thus, the hypotheses required to establish a separate Kolmogorov argument for universality of the cospectrum are of uncertain validity. This does not preclude a similarity of $Co_{w\theta}$, but it requires cautious interpretation of such similarity.

If we hypothesize that $Co_{w\theta}$ must scale with respect to individual properties of w and θ, then we may deduce a scaling for it from the known similarity of the other two variables. Recall that

$$E_{ww} = F(w)F(w)^*, \quad E_{\theta\theta} = F(\theta)F(\theta)^*, \tag{34}$$

where F denotes the Fourier transform and F^* its complex conjugate. Since E_{ww} and $E_{\theta\theta}$ are known to be similar with respect to an abscissa $\kappa\eta$ and ordinates scaled with

$$\frac{1}{\nu^{\frac{5}{4}}\epsilon^{\frac{1}{4}}}, \quad \frac{\epsilon^{\frac{3}{4}}}{\chi\nu^{\frac{5}{4}}} \tag{35}$$

respectively, it appears that $F(w)$ and $F(\theta)$ should be similar under $\kappa\eta$ and scalings of

$$\frac{1}{\nu^{\frac{5}{8}}\epsilon^{\frac{1}{8}}}, \quad \frac{\epsilon^{\frac{3}{8}}}{\chi^{\frac{1}{2}}\nu^{\frac{5}{8}}} \tag{36}$$

respectively. Appropriate averaging is implicit in the similarity, but we shall not attempt to work out the details here. The cross-spectrum is defined as

$$E_{w\theta} = F(w)F(\theta)^*, \tag{37}$$

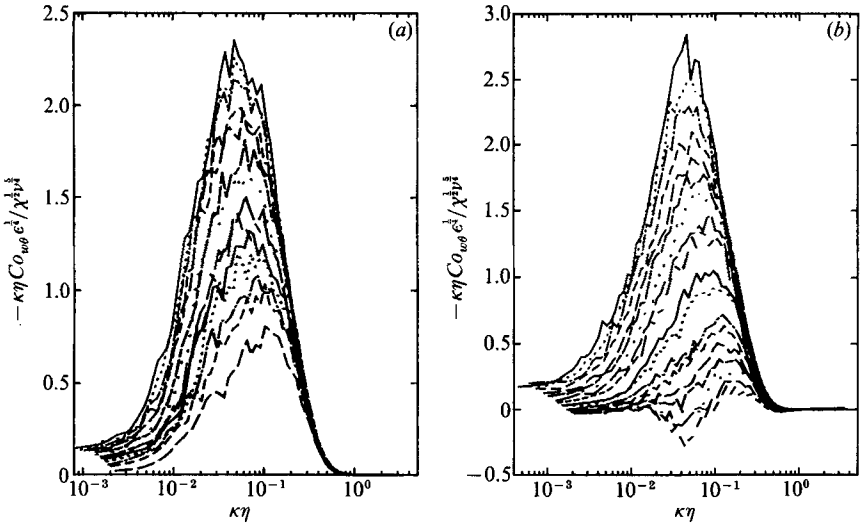

FIGURE 21. Universal cospectrum, $M = 5.08$ cm: (*a*) $N = 1.16$ s^{-1}, stations D–K′; (*b*) $N = 2.17$ s^{-1}, stations A**–K′.

so it would appear to have similarity in the sense of some universal function $F_{w\theta}$:

$$F_{w\theta}(\kappa\eta, Pr) = \frac{E_{w\theta}(\kappa\eta)\,\epsilon^{\frac{1}{4}}}{\chi^{\frac{1}{2}}\nu^{\frac{5}{4}}} \tag{38}$$

Figure 21 (*a*, *b*) shows cospectra under this scaling. The data are for stratifications of $N = 1.16$ s^{-1} and $N = 2.17$ s^{-1} ($M = 5.08$ cm) at 14 and 18 downstream stations, respectively (cf. figure 18*a*). The high-wavenumber data collapse beautifully. This universality may be extended to the phase as well, although the results are less interesting.

The wavenumbers which exhibit similarity are apparently relatively isotropic. As discussed in §2.2, this militates against significant molecular dissipation of $Co_{w\theta}$. A second conclusion is that we have accurately measured $Co_{w\theta}$ and $\overline{w\theta}$ over the range of interest, since an erroneous measurement (whose inaccuracy became severe above some frequency) would be unlikely to preserve this similarity.

The lower wavenumbers do not collapse in any sense under the universal equilibrium scaling. This is not unexpected. The low-wavenumber portion of the cross-spectrum is that associated with transport, and it is therefore an inherently anisotropic feature of the flow. Moreover, because the cospectrum is probably not characterized by a balance between large-scale production and small-scale molecular dissipation of $\overline{w\theta}$, the molecular dissipation rates used in the universal scaling are not proportional to the current level of $\overline{w\theta}$. This is in contrast to the velocity or scalar fields for which the variance is directly related to the dissipation rate via the energy cascade.

5.3. *Phase measurements*

While the cospectrum shows directly the spectral heat transport, it provides only inferential evidence of the degree of correlation of w and θ. It can go to zero if w and θ are uncorrelated in some bandwidth, but it can also go to zero if either w or θ goes to zero while the two remain essentially correlated. A more direct measure of the correlation of w and θ is the phase, $Ph_{w\theta}$.

The phase, $Ph_{w\theta}$ can be interpreted as the phase lag of θ behind w at any given

frequency. Several values of $Ph_{w\theta}$ are of special significance to us. If the flow field actively transports heat down the temperature gradient, then w and θ are $\pm 180°$ out of phase. (Whether the sign obtained is positive or negative here has no physical significance. It will depend only upon the location of the branch-cut for the arctangent function used to compute the phase. For the calculations presented herein, the branch-cut was placed along the negative imaginary axis, and active transport corresponds to $Ph_{w\theta} = 180°$. The specific position of the branch-cut is arbitrary and should be chosen so as to give continuous curves for $Ph_{w\theta}$.) A downward motion is associated with a positive temperature perturbation as it transports heat downward. If the flow field is restratifying, heat is carried against the temperature gradient. A downward motion is then associated with a negative temperature perturbation, and w and θ are in phase with one another.

The phase may also be used to detect the presence of internal waves, as suggested by Stewart (1969, p. 1273). Linear wave motions have no capacity to transport scalars. In a stably stratified environment, w is $+90°$ ahead of θ if the fluid motion is wavelike. Thus, the appearance of a bandwidth of $Ph_{w\theta} = +90°$ would indicate that the motion in that range was dominated by internal waves.

Figure 22(*a*) shows the phase for the passive and modestly suppressed regions ($t/\tau < 0.33$) of a strongly stratified flow. The vertical velocity fluctuation leads the temperature fluctuation by $+180°$ over the entire bandwidth, a condition of active turbulent transport; w and θ retain this phase relation through the early stages of the collapse of the heat flux. At the high wavenumbers, the phase decreases toward zero; in this range of scales the flow becomes isotropic, and w and θ become uncorrelated.

This and the subsequent graphs of the phase have been truncated in the early part of the isotropic region to avoid showing the noise-affected portions of the curves. This high-frequency error appeared to be more closely associated with the truncation error in the spectral calculations than with the frequency responses of the sensors. The phase is actually undefined in isotropic turbulence, but the ensemble-average phase difference is zero.

Figure 22(*b*) illustrates the effect of the large scales' collapse on the phase ($0.34 < t/\tau < 0.55$). The $+180°$ phase erodes, from the largest scales toward more intermediate scales, and collapses to 0°, thus displaying the countergradient heat transport on these scales. The region of zero phase lag between w and θ is coincident with that in which the cospectrum becomes positive (cf. figure 20), and its presence confirms our earlier conclusion that the large scales carry heat against the temperature gradient in this part of the flow.

A range of intermediate frequencies continue the normal turbulent transport of heat ($Ph_{w\theta} = +180°$) while the low frequencies collapse. At the highest wavenumbers, the turbulence becomes isotropic and the average phase again drops to zero. The cospectrum also vanishes in the isotropic region.

Figure 22(*c*) shows the phase development in the 'ringing' region of restratification overshoot ($0.57 < t/\tau < 0.8$). The phase lag of θ behind w increases from zero back to $+180°$, first at the largest scales but proceeding directly to the smaller restratifying scales. The entire bandwidth ultimately returns to the normal condition of cogradient heat transport. Apparently, once the flow has restratified, the turbulent mixing processes continue as in the initial stages of decay, but with smaller large eddies (as evidenced by the cospectra).

In none of our measurements was the phase observed to take on a value of $+90°$ over a measurable bandwidth. Thus, no bandwidth exhibits dominating characteristics of internal waves. However, an objection may be raised. To this point,

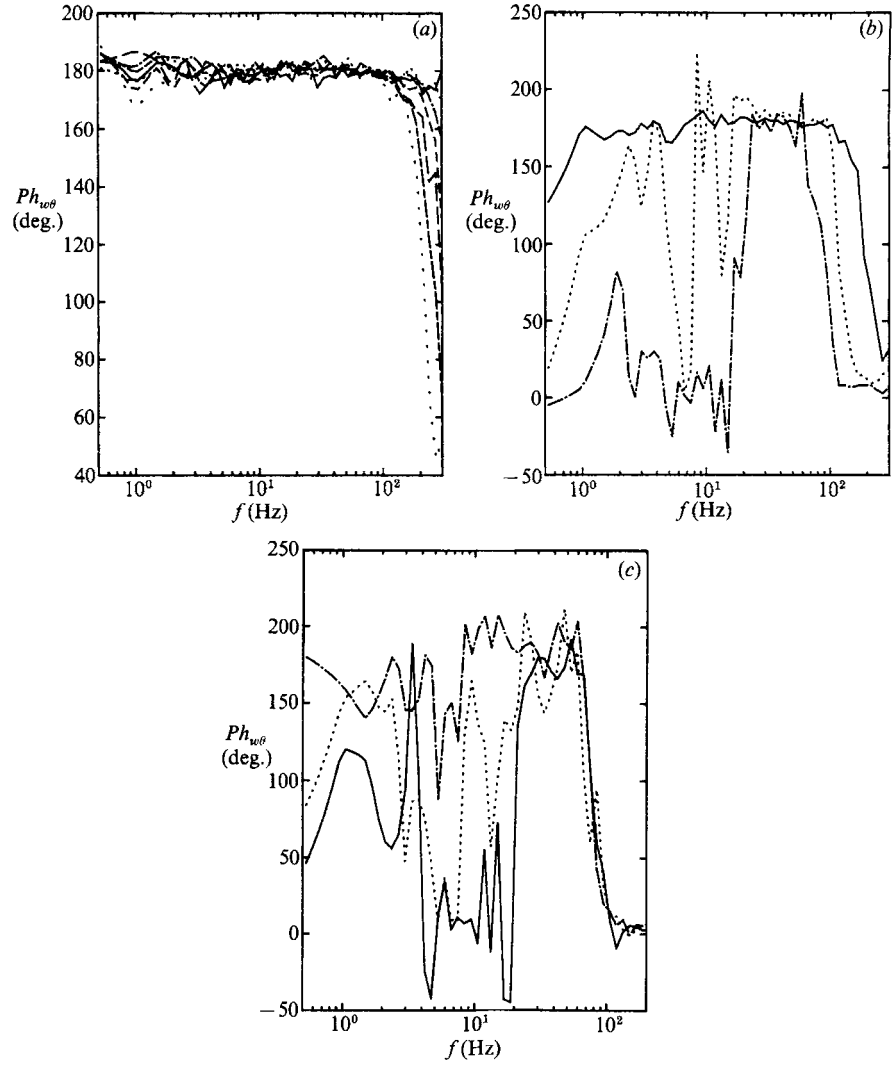

FIGURE 22. Phase for $N = 2.42\ \mathrm{s}^{-1}$ and $M = 5.08$ cm: (*a*) passive: A**–F*; (*b*) collapsing: —, F; ···, G; –·–, H; (*c*) overshoot: —, I′; ···, I; –·–, J.

our attention has been confined to frequencies above the Väisälä frequency of the flows, and the Väisälä frequency might be expected to retain the role of a cut-off frequency for internal waves that it has in fluids otherwise at rest. We cannot disallow internal waves fairly without considering the lower frequencies of the flow field.

5.4. *Low-frequency spectra*

Measurements of low-frequency spectra, from 0.0625 Hz to 100 Hz, were made at stations C, G, and J′. We now present some composite spectra, using these and the previous spectra to cover the entire bandwidth from 0.0625 Hz to 1000 Hz.

In figure 23 (*a*), the wideband power spectrum E_{uu} is shown at the three streamwise stations for $N = 0$. These spectra show a gradual rise in the region below 2 Hz, with a slope of about -0.4. The bulge at low frequencies decays at the same rate as the flat portion of the spectrum. Similar behaviour was seen in E_{ww}. Other studies in this

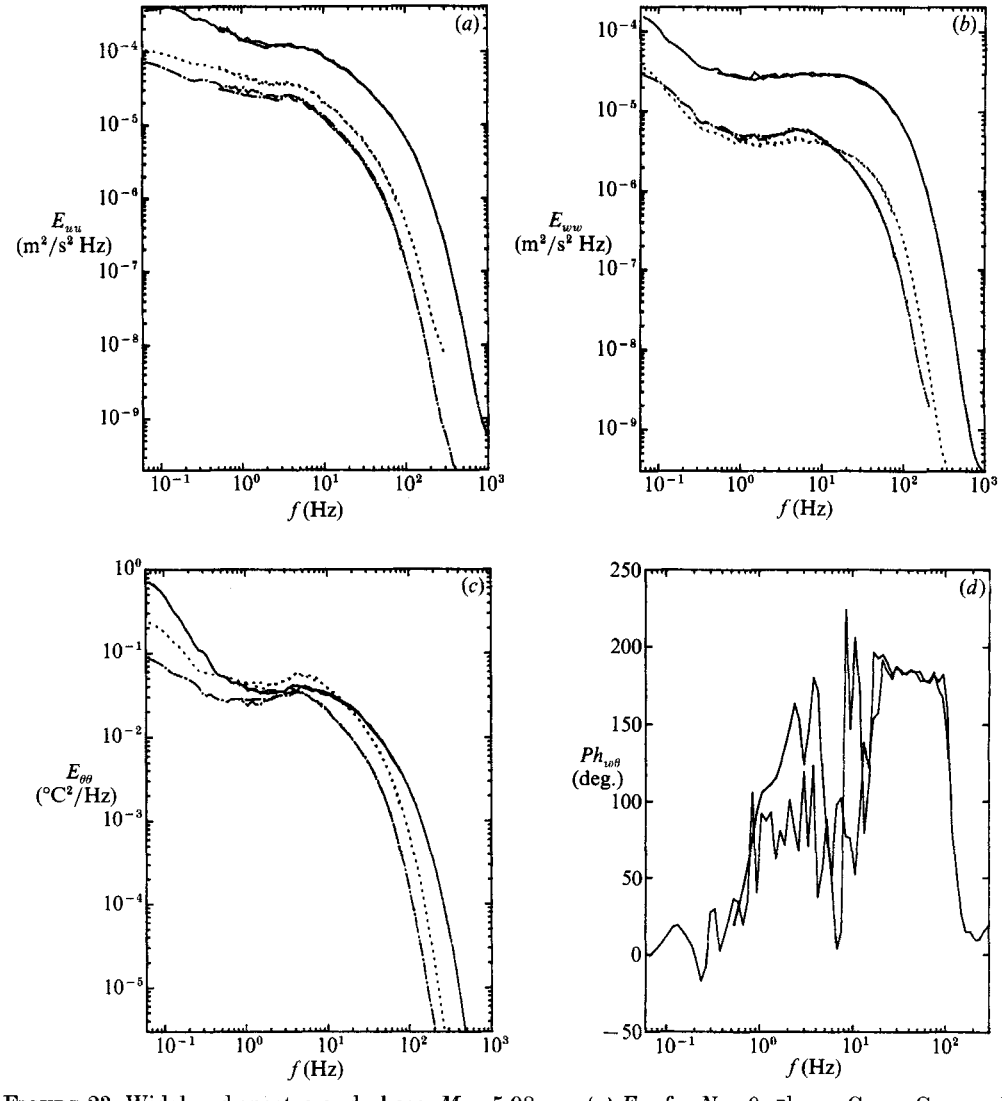

FIGURE 23. Wideband spectra and phase, $M = 5.08$ cm. (*a*) E_{uu} for $N = 0$ s^{-1}: —, C; ···, G; -·-, J′; (*b*) E_{ww} for $N = 2.42$ s^{-1}: —, C; ···, G; -·-, J′; (*c*) $E_{\theta\theta}$ for $N = 2.42$ s^{-1}: —, C; ···, G; -·-, J′; (*d*) $Ph_{w\theta}$ for $N = 2.42$ s^{-1}, station G.

wind tunnel (Helland & Van Atta 1978, figure 4) have revealed the power spectrum to rise continuously over the interval from 2 Hz down to 0.01 Hz. The rise is believed to be the result of long-period fluctuations in various environmental factors, such as the blower speed or the laboratory ventilation system.

Figures 23(*b*) and 23(*c*) show the power spectra E_{ww} and $E_{\theta\theta}$ when the flow is strongly stratified. The low-frequency rise in these spectra is somewhat more pronounced. For E_{ww} the slope of the rise is roughly -1.0, and it begins at about 0.8 Hz. The Väisälä frequency is less than this, about 0.39 Hz. The bulge in E_{ww} decays at the same rate as the flat portion of the spectrum. The rise in $E_{\theta\theta}$ is initially very steep, with a slope of about -2.0 below 1.0 Hz. However, this bulge decays faster than the flat portion of the spectrum and its slope decreases to about -0.4. The spectra of E_{uu} (not shown) are similar to the isothermal case.

A 'saturated' two-dimensional internal wave field should exhibit a spectral slope of -2 (Itsweire *et al.* 1986), but it is difficult to claim that this slope appears here. The rise in E_{ww}, which is of a lower slope, decays in conjunction with the other portions of the spectrum. It could equally well be a feature of the large-eddy structure of non-isothermal turbulence. The more pronounced rise in $E_{\theta\theta}$ decays significantly downstream. It is more likely associated with disturbances to the temperature field upstream of the grid; such a bulge would be expected to decay under the influence of buoyancy forces, whereas internal wave motions are thought to be more persistent. These rises are present in the unstratified case at about half the slope seen in the stratified case, and the change in slope is neither so sharp nor so close to the wave theory as to provide convincing support of it.

Conversely, these rises affect only w and θ, as would be expected for wave motions. The changes brought about by stratification are in the same direction as would be expected for a wave field. One could view the bulges as being the result of a relatively weak internal wave motion. The cause of these slight increases in the low-frequency slope of the spectra is thus highly equivocable at this juncture. Let us now consider the phase.

Figure 23(*d*) shows the wideband phase measurement at station G for the non-isothermal power spectra just discussed. Even at the low frequencies associated with internal waves and the observed bulges, the phase is never $+90°$. Yet, the bulges seen in the power spectra amount to an increase in energy of as much as a factor of ten over that of flat spectra. If the bulges were produced by internal wave motions, then internal wave motions would dominate E_{ww} and $E_{\theta\theta}$ in the bulge bandwidth; and if E_{ww} and $E_{\theta\theta}$ were primarily supported by wave motions in that bandwidth, then the phase measured would be $+90°$.

The phase measured at low-frequency is actually entirely consistent with the turbulence and restratification ideas previously discussed. While those ideas do not contradict the wave concept, little justification exists for the introduction of a wave model in the present context. The bulges seen in the low-frequency power spectra could equally well be caused by the large-scale features of the noise from upstream of the grid.

Internal waves thus appear to have no significant role in the dynamics of the present flows. All behaviour of u', $w'\,\theta'$, and $\overline{w\theta}$ can be explained without reference to them; and the phase measurements oppose them. Internal waves are a low-frequency phenomenon. In a fluid at rest, they are damped exponentially at frequencies above the Väisälä frequency. (Travelling internal waves, a mean flow, and the assorted generating and forcing mechanisms present make one wary of applying too much generality to this idea. An open problem for analysis is to determine what sort of wave field is permitted in such laboratory flows and what its one-dimensional frequency spectrum might be.) Thus, the scales at which most turbulent processes occur and the scales at which we expect internal waves are fundamentally separated. How small-scale turbulence may transfer energy to the larger scales of wave motions is not presently understood. Wave motions may possibly be generated by other agencies, and, as the turbulence decays, these wave motions may remain active. But the dynamics of the turbulence do not seem to be strongly related to the presence or absence of internal waves: waves would be superfluous if given much weight in the present context.

One possible reason for the apparent absence of internal waves in the present flows, as compared to the salt-water channel flows, is that the stratified wind tunnel was designed to be supercritical with respect to standing internal wave motions. Such a

constraint was not applied to the water channel design. Hence, the present flows lack a background wave field which may have been present in the other flows. Additionally, the higher rate of scalar dissipation in air flows consumes buoyant potential energy almost as fast as it is created (see figure 14), reducing the driving force for waves, again in contrast to the salt-stratified case.

6. Lengthscale relations

6.1. *General features of scale evolution*

We now consider the two physical lengthscales, L_t and L_b, as well as three scale estimates, the Kolmogorov scale η, the Obukhov–Corrsin scale η_θ, and the Ozmidov scale, $L_O = (\epsilon/N^3)^{\frac{1}{2}}$. The Ozmidov scale is that at which buoyant and inertial forces are approximately equal; it has been widely used in studies of stratified turbulence. The lengthscales are shown for the 5.08 cm grid at stratifications of 1.16, 1.49, 2.17, 2.42 s^{-1} in figure 24.

The initial separation of the molecular scales, η and η_θ, from the thermal overturning scale, L_t, represents the range of turbulent scales initially present. The molecular scales grow monotonically downstream, as the turbulence becomes less vigorous. The overturning scale grows somewhat more slowly. However, the scales always remain separated and there is thus always a range of scales between the molecular and overturning scales which is actively turbulent.

The dissipation rate is only weakly affected by the presence of stratification and the molecular scales, which vary as $\epsilon^{-\frac{1}{4}}$, are even more weakly affected. The difference in η for various stratifications arises because the flow with $N = 2.42$ s^{-1} had a lower mean speed; this causes η to be larger for the more heavily stratified case. The other scales show a similar response.

The most intriguing behaviour to be found on these graphs is the role of L_b as an exact upper bound on L_t. In each case, L_t grows until it equals L_b and then decays with it. In the most heavily stratified cases, the decay of L_b slows when the region of restratification overshoot is reached, while L_t continues to decay. We have previously discussed the relationship of these scales (see especially figure 3), but it is worthwhile to say a little more.

The buoyancy scale, L_b, is the maximum r.m.s. displacement that can be produced from a given r.m.s. kinetic energy, and, to a reasonable approximation, this limit is physically realized: the variance-producing scales,which L_b characterizes, are essentially free of viscous effects, and dynamic pressure effects on these scales may also be negligible compared with buoyant pressure effects. Under these assumptions, L_b is a direct limit on the r.m.s. vertical displacement of particles from their instantaneous equilibrium locations, L_t.

From §1, the ratio of L_b and L_t can be related directly to the turbulent energies:

$$\frac{\overline{T}}{\overline{\Psi}} = \left(\frac{L_b}{L_t}\right)^2. \tag{39}$$

Hence, we can add an energetic interpretation of the ratio L_b/L_t to those given in §2.2. As the turbulence decays and the particles disperse farther, the initially large ratio of kinetic to potential energy declines. Less kinetic energy is available to support the particle displacement, and buoyancy forces drive particles back toward their equilibrium positions. Once the r.m.s. kinetic energy equals the r.m.s. potential energy, further vertical dispersion appears to be impossible because the kinetic

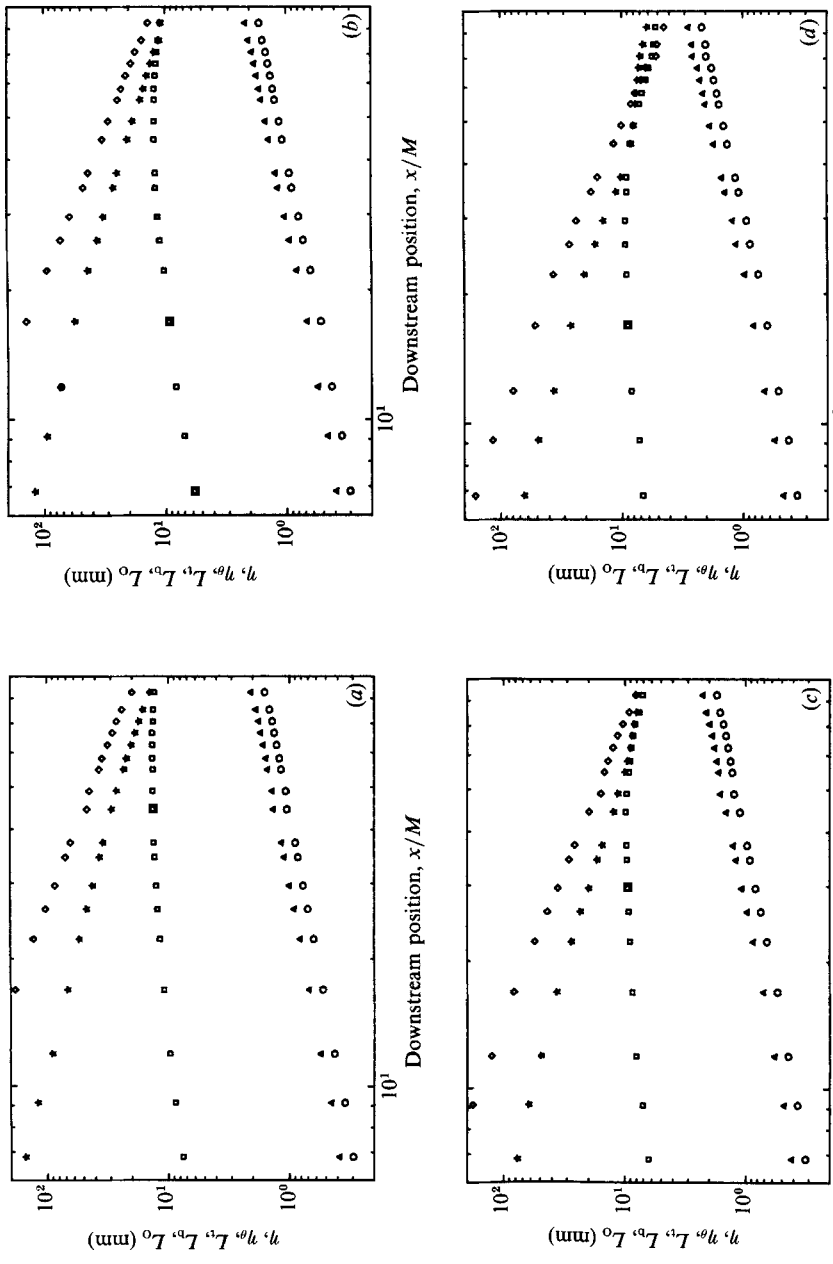

FIGURE 24. Lengthscale maps, $M = 5.08$ cm: (*a*) $N = 1.16\ \mathrm{s}^{-1}$; (*b*) $N = 1.49\ \mathrm{s}^{-1}$; (*c*) $N = 2.17\ \mathrm{s}^{-1}$; (*d*) $N = 2.42\ \mathrm{s}^{-1}$. ○, η; △, η_θ; □, L_t; ★, L_b; ◇. L_o.

energy is not sufficient to sustain any additional potential energy. (Evidently, scalar variance does not survive well in the absence of active stirring in thermally stratified air.) Hence, the ratio L_b/L_t does not fall below unity. In the region of restratification overshoot, the ratio grows as stored potential energy is converted back to kinetic energy.

A final observation in regard to these lengthscale maps is that the buoyancy scale seems to have far more relevance to the development of the turbulence than does the Ozmidov scale. The Ozmidov scale has often been used in characterizations of the point at which buoyancy and viscous scales are equal. We consider that type of transition next.

6.2. *Flow transitions and fossilization*

For the range of development seen in this study, the buoyancy scales never become as small as the molecular scales, and the flow does not reach a state in which all scales of the motion are suppressed by buoyancy. That state, referred to as *fully fossilized* turbulence (Gibson 1980), is believed to be much more significantly affected by internal waves. It is also believed to be well characterized by various ratios of lengthscales, in particular, that of the Ozmidov scale to the Kolmogorov scale. The length of the present test section is not sufficient to reach the fossilized state and the data can support no firm conclusions with respect to a fully fossilized turbulence.

Discussions of the development of stratified turbulence often use the idea of an onset of buoyancy effects followed by a final extinction of turbulent overturning (fossilization). Onset is generally defined by the appearance of retarded development of L_t and extinction by the criterion $\overline{w\theta} \approx 0$. In the present flow, onset is most sharply defined with respect to w', but may be described in terms of several other variables, as well (see below). The extinction criterion, $\overline{w\theta} \approx 0$, was shown to be inadequate in §5, and the cross-spectral data suggest that the present flows always have a range of active turbulence. Thus, we cannot meaningfully present quantitative criteria for extinction.

However, we are in a position to develop upper bounds on some of the pertinent fossilization relationships. At the test-section end, for the most heavily stratified run

$$L_O/\eta = 2.06. \tag{40}$$

This ratio decreases monotonically downstream, so that the present value is an upper bound on that expected for fossilized turbulence. It is to be compared with values of 7.63 and 9.86 measured by Itsweire *et al.* in salt water. At the point where $\overline{w\theta} = 0$ (which we recognize as actively turbulent), the dissipation rate is related to the Väisälä frequency by

$$\epsilon = 8.73\nu N^2, \quad \epsilon = 8.77\nu N^2 \tag{41}$$

for $M = 5.08$ cm with $N = 2.42\ \mathrm{s}^{-1}$ and $N = 2.17\ \mathrm{s}^{-1}$, respectively. Since ϵ decays monotonically downstream, the constants in these relations represent upper bounds on those that would be found at the point when all active turbulence is arrested. These values may be compared to the value of 30 predicted by Gibson (1980) and the values of 15 and 21 measured by Itsweire *et al.* in salt water.

It would appear that the Prandtl number significantly influences ratios of this type. A second difficulty with assigning much generality to such ratios is that the local structure of decaying turbulence at any time is dependent on its previous history: the process is, after all, unsteady. The primary value of such ratios would appear to be as qualitative gauges of relative separation of scales.

The last two types of scale relations we consider are relevant to the onset of buoyancy effects, which we take to occur at the first station for which w' shows a

N (s^{-1})	Station	t/τ	L_O/L_t	L_b/L_t	$\epsilon/\alpha CoN^2$
2.42	C	0.158	5.76	2.94	38.49
2.17	D	0.162	6.11	3.03	38.55
1.49	E′	0.127	6.56	3.27	39.19
1.16	E	0.113	6.80	3.34	38.90

TABLE 8. Scale ratios at onset of buoyancy effects: $M = 5.08$ cm

significant departure from passive development ($g(t/\tau) > 1.10$). One relation is the ratio of the buoyancy or the Ozmidov scale to the thermal overturning scale at onset (table 8). The average ratios for the two lengthscales are

$$L_O = (6.31 \pm 0.46) L_t, \quad L_b = (3.15 \pm 0.19) L_t, \tag{42}$$

as compared to the ratio $L_O = 1.18 L_t$ measured by Itsweire *et al.* The separation of scales at onset is much larger for temperature-stratified air than for salt-stratified water.

The other scale relationship relevant to the onset of fossilization is that between ϵ and the scalar dissipation rate in the form of αCoN^2. These values are cross-plotted in figure 25 for several stratifications and the 5.08 cm grid. Gibson (1980, 1982) has given theoretical arguments that the two dissipation rates should be related at the onset of buoyancy effects by

$$\epsilon_0 = (4\text{–}15)\, \alpha CoN^2, \tag{43}$$

where the constant of proportionality lies in the range given, and may have the specific value of 13. The line obtained using the constant 13 is shown on the figure. Also shown is the experimentally determined line for onset:

$$\epsilon_0 = (38.78 \pm 0.33)\, \alpha CoN^2. \tag{44}$$

This line was calculated from the data in table 8, which reference 'onset' to the departure of w' from passive behaviour. The experimental line differs considerably from the prediction. It could conceivably be lowered toward the predicted line by using a more lenient criterion for the onset of buoyancy effects, such as the appearance of restratification.

Such a criterion is not unreasonable. Buoyancy clearly acts continuously on the vertical motion of particles; it does not simply commence at some point in time. When using a criterion that is based on departure from passive scalar growth, we are merely quantifying the integrated effects of buoyancy on the structure of the turbulence. The alternative of using restratification to gauge onset of buoyancy effects is attractive because it shows the point at which the turbulence loses its capacity to disperse particles vertically. The appearance of restratification may be taken to be the point at which $L_b/L_t = 1$; this criterion is chosen for convenience, and is also indicative of the appearance of countergradient transport in the cross-spectral data. Calculating the appropriate ratio at each station which reaches this level of development (specifically, at the first station at which L_b/L_t is less than 1.05) yields the line

$$\epsilon_{\text{restrat}} = (6.18 \pm 0.29)\, \alpha CoN^2. \tag{45}$$

This line is not shown in figure 25, but does lie within Gibson's predicted range.

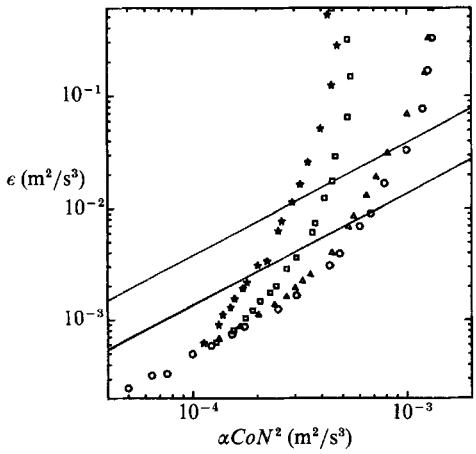

FIGURE 25. Dissipation rate relations, $M = 5.08$ cm: ○, $N = 2.42$ s^{-1}; △, $N = 2.17$ s^{-1}; □, $N = 1.49$ s^{-1}; ★, $N = 1.16$ s^{-1}.

t/τ	L_b/L_t	Observed effects
0.1	4.5	w' shows accelerated decay
0.15	3.0	$\overline{w\theta}/w'\theta'$ erosion starts; L_t growth slows; low-frequency decay of $Co_{w\theta}$
0.32	1.18	L_t ceases to grow
0.35	1.10	$Ph_{w\theta}$ shows first low-frequency decrease
0.40	1.00	$L_b = L_t$; $g(t/\tau)$ reaches its maximum value; streamwise heat flux begins to decay
0.45	1.00	$Ph_{w\theta} = 0$ for some frequencies
0.52	1.03	$L_b > L_t$
0.55	1.07	$\overline{w\theta}/w'\theta'$ reaches its minimum; $Ph_{w\theta} = 0$ on a wide bandwidth
0.60	1.15	$\overline{w\theta}/w'\theta'$ and $Ph_{w\theta}$ increase; $g(t/\tau)$ levels out; $L_O = L_t$
0.64	1.20	$L_t > L_O$
0.70	1.20	$Ph_{w\theta} \approx 180°$ at all frequencies

TABLE 9. The development of stratified turbulence

6.3. *Flow development with t/τ*

We may summarize the turbulent evolution in terms of increasing dimensionless time, t/τ (table 9). The numerical values given are averages.

The passive behaviour occurs only for $t/\tau < 0.1$–0.15; large-scale buoyancy effects appear for $t/\tau > 0.15$. In the range $0.3 < t/\tau < 0.4$, the vertical particle dispersion is fully arrested, rather than merely retarded. From $t/\tau = 0.45$ to $t/\tau = 0.55$, the flow shows large-scale restratification. Beyond $t/\tau = 0.55$, the restratification overshoot appears as large scales return to normal turbulent behaviour.

Onset of buoyancy effects can be defined either as the first appearance of buoyancy-driven change in the flow ($t/\tau = 0.1$) or as the point at which restratification becomes significant ($t/\tau = 0.4$, say). In the light of the continuous action of buoyancy on the flow field, the simple concept of 'onset' seems a bit vague; the approach of specifying times for the occurrence of some specific effect, as in table 9, seems preferable.

The large, variance-producing scales show unsteadiness in conjunction with the basic downstream decay of the flow and cannot be regarded independent of past

history. Thus, it seems unlikely that specific features of an arbitrary stratified turbulent flow can be expected to occur at the same values of length- or timescale ratios as in stratified grid turbulence. Caution is advised when quantitatively extrapolating the present data to other flows.

7. Comparison to other works

While the present experiments are unique in being the only experiments to produce dynamically active buoyancy forces in a continuously stratified turbulent wind tunnel flow, a variety of related studies provide interesting comparisons and contrasts. We now consider theoretical models, experiments in passively stratified turbulent air flows, numerical simulations, and experiments in strongly stratified turbulent salt-water flows, giving particular attention to the consequences of varying the Prandtl number.

7.1. *Theoretical models*

Dunn & Reid (1958) and Deissler (1962) solved the moment equations, assuming Re_λ to be sufficiently small that the inertial energy transfer terms can be neglected. Dunn & Reid suggest that Re_λ as high as 5 might be sufficiently small for quantitative accuracy. Qualitative accuracy may apply to even higher values.

Dunn & Reid considered isotropic, low-Reynolds-number turbulent flow, assuming the flow field to be unaffected by the temperature field (thus $N \rightarrow 0$) and taking the mean temperature to have a constant gradient in one direction. They found that $\overline{\theta^2}$ has a strong dependence on Pr, both statistically and spectrally. Conversely, the heat transfer correlation coefficient, $\overline{w\theta}/w'\theta'$, was found to be less sensitive to Pr. The basic effect of increasing Pr from values appropriate to air to values appropriate to salt water was to shift the spectral distributions of $\overline{w\theta}/w'\theta'$ and $\overline{\theta^2}$ to smaller scales. These trends are generally the same as those observed in this work, although not quantitatively applicable to it.

Deissler extended this type of analysis to include a body force antiparallel to the mean temperature gradient. Of particular importance are his predictions of the cospectrum of the vertical heat flux, $Co_{w\theta}$. For $Pr = 0.7$, the predicted cospectra decay to show a distinct countergradient transport at the large scales while the small scales continue to transport heat actively; this behaviour is identical to that discussed in §5.1.

Deissler's cospectral curves are reproduced in figure 26 for Prandtl numbers of 0.7 and 10.0 at various values of the buoyancy time, Nt. A remarkable difference between the curves for the two values of Prandtl number is that the countergradient transport is shifted to high wavenumbers for the high-Prandtl-number case. The reason for this shift appears to be a corresponding shift of the temperature variance to higher wavenumbers (see Deissler's figure 6*b*). In the light of the relatively poor high-wavenumber resolution of the salt-water experiments, the absence of restratification in the cospectra of Itsweire *et al.* (1986) should be re-examined using finer experimental techniques.

Deissler's computations also show that the decay of $\overline{w\theta}/w'\theta'$ with increasing buoyancy time is significantly greater at high Pr than at low Pr (see his figure 8). This trend is consistent with the observed differences in the development of $\overline{w\theta}/w'\theta'$ for the air and salt-water experiments.

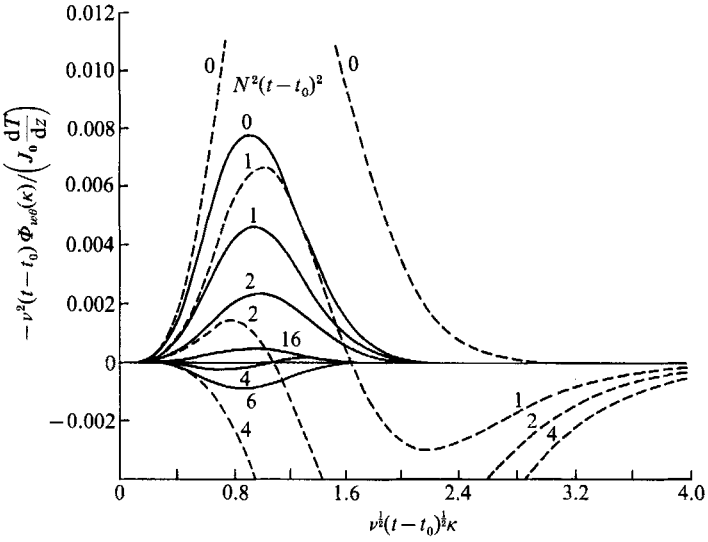

FIGURE 26. Deissler's three-dimensional cospectra. (J_0 is a spectral constant indicative of the initial turbulence intensity.) ——, $Pr = 0.7$; – – –, $Pr = 10.0$.

7.2. *Passively stratified experiments*

We may compare our results to passively stratified experiments in order to check our initial conditions and to test the extent to which previous studies were passive. Table 10 presents selected quantities measured in several studies of passively stratified air flow. For the works of Sirivat & Warhaft (1983), Venkataramani & Chevray (1978), and Wiskind (1962) the table includes only the data for the largest values of t/τ measured (Sirivat & Warhaft used two different heating configurations). For the data of Montgomery (1974), we have presented all measurements of $\overline{w\theta}/w'\theta'$.

The measured values of $\overline{w\theta}/w'\theta'$ are in good agreement with the data of the present study for small values of t/τ. An exception occurs for the single point measured by Wiskind (-0.48) which is lower than in all other investigations; the cause of this discrepancy is unclear. For most of these experiments, t/τ is small enough that the entire data set should be contained within the region found to be passive in the present study; and, with the exception of Montgomery, none of these investigators reported any buoyant suppression of the vertical kinetic energy or the scalar dispersion.

In Montgomery's most heavily stratified run ($N = 1.08\ \mathrm{s}^{-1}$), the vertical r.m.s. velocity w' shows a distinct decrease from its isothermal values over the entire length of the tunnel. This result is very surprising, since it is only at the very end of Montgomery's test section that t/τ becomes large enough that buoyancy effects might be expected on the basis of the present experiments ($t/\tau < 0.13$ for all of his data). None of Montgomery's data show any decrease in the growth rate of θ'; this is as would be expected for the small buoyancy times considered.

All of the studies of passively stratified flow (the present study being no exception; see Lienhard 1988) make much of the fact that the linearity of the mean profile is preserved as the flow moves downstream ('thus verifying Corrsin's (1952) prediction'). However, we ought to keep that behaviour in perspective. The preservation of the mean gradient is simply a consequence of energy conservation

Investigator	dT/dz (°C/m)	N (s^{-1})	U (m/s)	M (cm)	x/M	Re_λ	t/τ	$\overline{w\theta}/w'\theta'$
Montgomery	18	0.77	6.1	2.54	72	35	0.037	−0.63
	18	0.77	6.1	2.54	180	35	0.092	−0.68
	36	1.08	6.1	2.54	72	35	0.052	−0.63
	36	1.08	6.1	2.54	180	35	0.129	−0.64
Sirivat & Warhaft	8.1	0.51	3.4	2.5	150	26.4	0.093	−0.7
	10.3	0.58	6.3	2.5	150	36.5	0.055	−0.68
Venkataramani & Chevray	9.94	0.58	8.16	3.81	49.2	64.4	0.021	−0.61
Wiskind	25	0.90	6.8	2.54	102	30	0.055	−0.48

TABLE 10. Data from passive experiments

and the homogeneity of the flow field. The only mechanisms that can destroy the mean profile are the heat loss and inhomogeneity found at the boundaries of the flow.

7.3. *Numerical simulations*

Some recent studies present full numerical implementations of the Navier–Stokes equations for stratified homogeneous turbulence at Reynolds numbers similar to those of the present work. However, detailed comparisons are difficult in some cases as a result of either the initial conditions or the scalings of the simulations.

Sanderson, Hill & Herring (1987) used the direct interaction approximation to compute various statistical quantities at a Prandtl number of 0.7 and observed the same type of suppression of vertical kinetic energy and scalar growth as seen here. Riley, Metcalfe & Weissman (1981) used a pseudo-spectral implementation to solve the equations of motion at a Prandtl number of 0.7 (J. Riley, personal communication, 1987). Their Re_λ was 27.2 and they used several stratifications. They found qualitatively similar behaviour of $\overline{\rho w}$ and saw a marked acceleration of the decay of w' in the presence of buoyancy forces. The r.m.s. kinetic energy always exceeded the r.m.s. potential energy in their simulations.

Métais (1987) and Métais & Herring (1989) used direct simulation with initial conditions similar to those of Itsweire *et al.* (1986) at $Re_\lambda = 40$, $N = 0.98\ s^{-1}$. They found favourable comparisons of Itsweire *et al.*'s u', w', and θ' development to calculations at $Pr = 1$. Like Itsweire *et al.*, they observed the r.m.s. potential energy to exceed the kinetic energy at some downstream position, in contrast to the present data. Their simulations showed wave-like behaviour for very large values of t/τ. Apparently, the difference in Pr does not affect these particular statistics significantly.

Métais & Herring (and also O. Métais, personal communication, 1987) present some data on the effect of varying Pr. They compute the vertical heat flux correlation coefficient for several Prandtl numbers and find definite variations in $\overline{w\theta}/w'\theta'$. In particular, the data of Itsweire *et al.*, which is for a Schmidt number of about 500, show a significantly lower amplitude of variation than the computed values for $Pr = 1$. The computed range of Pr, 0.6 to 2.0, shows an increase in $\overline{w\theta}/w'\theta'$ with increasing Pr, but the trend may reverse for larger Pr. The computed curve for $Pr = 1$ is compared to the present data and the Itsweire *et al.* data in figure 27.

7.4. *Salt-water experiments*

The salt-water experiments of Stillinger *et al.* (1983*b*) and of Itsweire *et al.* (1986) may

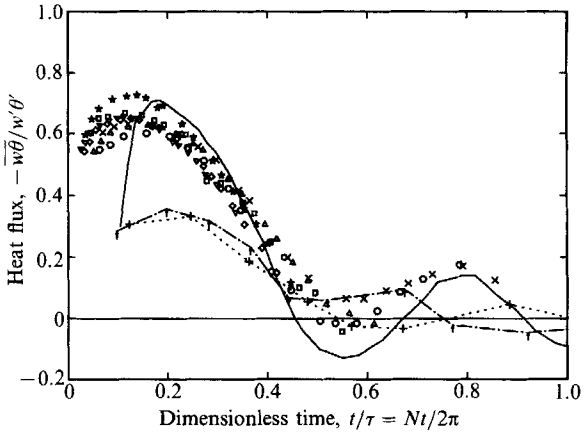

FIGURE 27. The effect of Prandtl number on vertical transport: —, Métais & Herring, $Pr = 1$, $N = 0.98\ \mathrm{s}^{-1}$; ···+···, Itsweire *et al.* R37, salt water, $N = 0.98\ \mathrm{s}^{-1}$; –·–↑–·–, Itsweire *et al.* R37, salt water, $N = 0.74\ \mathrm{s}^{-1}$; other symbols, present data.

be directly compared to the present experiments. A number of such comparisons have already been made above.

Perhaps the most striking difference from the salt-water studies is the apparent absence of internal waves in the air experiments. The possible reasons for the lack of any wave field are discussed in §5.4. This wavelessness may also explain why the velocity field in the present experiments showed such consistent and predictable behaviour in comparison to the behaviour of u' and w' in the Stillinger *et al.* and Itsweire *et al.* experiments.

The salt-water experiments reported failure of universal equilibrium scaling at high wavenumbers for large values of the buoyancy time. Such a failure was not observed in the present data. This difference is probably a consequence of another major difference between the present work and the salt-water works: the salt-water data appear to show fossilization of the turbulence. In the air data, the flow remains actively turbulent at the small scales for all points measured. The presence of active small-scale turbulence appears responsible for the continuing isotropy of the smallest eddies.

Another major difference is the rather diffuse appearance of buoyancy effects in the air data as compared to the sharp transitions seen in the salt-water data, particularly in L_t. This difference is most likely the result of the greater role of molecular diffusion in the scalar development in air.

The air data have a great advantage over the salt-water data in their higher levels of statistical and spectral resolution and accuracy. The salt-water data show very little direct spectral evidence of the restratification inferred from the scalar development. The air data, having much better cross-spectral and small-scale resolution, demonstrate the presence of restratification very clearly. Various statistical quantities which did not scale well in the salt-water data (such as $\overline{pw}$) collapse neatly for the air data. This is not to denigrate the salt-water experiments: salt water is a difficult medium to study quantitatively.

7.5. *The role of the Prandtl number*

The preceding comparisons indicate that the Prandtl number strongly affects the behaviour of stratified turbulence. An increasing Prandtl number reduces the

molecular diffusion of the scalar relative to the turbulent stirring of the flow. Thus, the scalar variance in a high-Prandtl-number fluid is almost unaffected by dissipation, and as a result its development is more sharply affected by the appearance of large-scale buoyancy forces. The persistence of the scalar fluctuations may also be responsible for the ability of the r.m.s. potential energy to exceed the r.m.s. kinetic energy in salt water; in air, the scalar fluctuations are diffused more rapidly and must be sustained by a continuous input of kinetic energy.

Another consequence of the lesser molecular diffusion at high Pr is that a turbulent scalar has significant fluctuations at increasingly high wavenumber as the Prandtl number increases. This change appears to shift the range of scales which restratify relative to the peak of the turbulent velocity spectrum, in turn shifting the range of scales on which the cospectrum shows countergradient transport from scales larger than the peak of $Co_{w\theta}$ for Pr near unity to scales smaller than the peak for high Pr.

The heat flux correlation coefficient, $\overline{w\theta}/w'\theta'$, is also subject to Prandtl-number effects. For the high Schmidt numbers found in salt water, it is initially some 30% less than in air and develops to show a more pronounced range of t/τ having net countergradient transport (figure 27). This difference results from the greater role of molecular diffusion in air as compared to salt water. As we have seen, scalar variance is rapidly dissipated in the present flows and persists only through ongoing vertical turbulent mixing. Thus, w and θ must be strongly correlated at low Prandtl number. Conversely, at high Prandtl (or Schmidt) number, scalar fluctuations are dissipated much less rapidly than velocity fluctuations. Hence, a fluid particle's position relative to its position of buoyant equilibrium is not as well correlated with its present vertical velocity, and $\overline{w\theta}/w'\theta'$ is smaller. The greater range of countergradient transport at high Pr also results from the lesser dissipation of the stored potential energy (i.e. scalar variance) which drives restratification.

8. Summary

The decay of grid-generated turbulence is studied in the presence of strong buoyancy forces. A novel air flow facility has been used to produce the highest stable stratifications obtained to date in a continuously stratified air flow and stratifications as high or higher than have been obtained in continuously stratified salt-water flows. A large statistical database has been obtained which provides considerable insight to the structural and transport properties of thermally stratified turbulence.

The evolution of the turbulent velocity field in these air data is far more coherent than were such measurements in water. In part, that is attributable to the better instrumentation available here, and, in part, it results from the apparent absence of internal waves in the present test section. As a consequence, the present data yield an intricate portrait of the structural evolution of stratified turbulence which was not previously available.

Buoyancy forces strongly retard the vertical dispersion of fluid particles, causing marked reductions in the vertical kinetic energy and in the vertical transport of heat. The declining transport in the flow is found to be related to the levels of r.m.s. kinetic and potential energy characterized by the buoyancy scale, L_b and the overturning scale, L_t, respectively.

The data show the distinct appearance of a two-scale behaviour of the turbulent field. Cospectra and phase of the vertical transport cross-correlation show that large scales of motion come to be dominated by buoyancy forces and restratification processes, while the small scales remain actively turbulent. Universal equilibrium

scaling remains valid for the high wavenumbers of the velocity and temperature spectra, suggesting the continuing isotropy of these scales in spite of the developing anisotropy of the large scales of the flow field. An original universal equilibrium scaling is derived for the cospectrum and is verified using the present experimental results.

The two-scale structure of the turbulence is used to construct a scaling for the flow development. This scaling uses a buoyancy timescale (non-dimensionalized with the Väisälä period) and separate scales representative of viscous decay processes. Under these scalings, universal curves are obtained for the decay of the vertical heat transport, the decay of the vertical kinetic energy, the development of the scalar variance (as L_t/L_b), and for the effect of buoyancy on the viscous and scalar dissipation rates. The universal scaling of the kinetic energy decay, in particular, is an entirely unexpected new result which derives from the highly consistent measurements possible in the present air flows.

No discernible internal wave effects were found. The turbulent intensities evolve consistently and in a fashion explicable in terms of the turbulent kinetic energy balances. Similar statements apply to the scalar development. The spectral development shows no clear evidence of internal waves, either, and phase measurements also contradict a wave hypothesis. This is in contradistinction to the observed behaviour in salt-stratified flows.

Comparison to other studies suggests that the Prandtl number significantly affects the structure of stratified turbulence. The greater role of molecular dissipation in air as compared to salt water leads to numerous differences from previous salt-stratified experiments. Its influence is particularly apparent in the statistical and cospectral behaviour of the vertical transport and in the scalar variance and spectra.

These results constitute a significant departure from previous notions about the evolution of stratified turbulence, which were largely based on salt-stratified water data. The flow does not evolve in a series of distinct transitions. Buoyancy forces, which are continuously present, have a continuous effect on the flow field. The suppression of turbulent stirring by buoyancy forces does not simply stop vertical transport at all scales below a critical one, but induces a large-scale restratification in the presence of continued small-scale turbulence. Consequently, the vanishing of the vertical heat transport is not a sufficient condition for the extinction of turbulent motion, as was previously assumed. Additionally, turbulent motion appears to have no ability to generate waves on the range of scales encountered here. In the light of the present data, many of the results and conjectures of the salt-water experiments must be reassessed, particularly before being applied to flows at lower Prandtl number.

The authors wish to thank Dr K. N. Helland who contributed much to the formative stages of this work. This study was supported by the National Science Foundation under grant numbers OCE82-05946 and OCE85-11289 with partial support from DARPA grant number N00014-86-K-0758 and ONR URI contract number N00014-86-K-0690, 'From mixing to Mesoscale'.

REFERENCES

BATCHELOR, G. K. 1953 *The Theory of Homogeneous Turbulence*. Cambridge University Press.

BATCHELOR, G. K. 1959 Small-scale variation of convected quantities like temperature in turbulent fluid. *J. Fluid Mech.* **5**, 113–133.

BRITTER, R. E., HUNT, J. C., MARSH, G. L. & SNYDER, W. S. 1983 The effect of stable stratification on turbulent diffusion and the decay of grid turbulence. *J. Fluid Mech.* **127**, 27–44.

CORRSIN, S. 1951*a* On the spectrum of isotropic temperature fluctuations in an isotropic turbulence. *J. Appl. Phys.* **22**, 469–473.

CORRSIN, S. 1951*b* The decay of isotropic temperature fluctuations in an isotropic turbulence. *J. Aeronaut. Sci.* **18**, 417–423.

CORRSIN, S. 1952 Heat transfer in isotropic turbulence. *J. Appl. Phys.* **23**, 113–118.

DEISSLER, R. G. 1962 Turbulence in the presence of a vertical body force and temperature gradient. *J. Geophys. Res.* **67**, 3049–3062.

DICKEY, T. D. & MELLOR, G. L. 1980 Decaying turbulence in neutral and stratified fluids. *J. Fluid Mech.* **99**, 13–31.

DUNN, D. W. & REID, W. H. 1958 Heat transfer in isotropic turbulence during the final period of decay. *NACA TN*-4186.

GARGETT, A. E. 1985 Evolution of scalar spectra with the decay of turbulence in a stratified fluid. *J. Fluid Mech.* **159**, 379–407.

GEORGE, W. K., BEUTHER, P. D. & ARNDT, R. E. A. 1984 Pressure spectra in turbulent free shear flows. *J. Fluid Mech.* **148**, 155–191.

GIBSON, C. H. 1980 Fossil temperature, salinity, and vorticity in the ocean. In *Marine Turbulence* (ed. J. C. T. Nihoul), p. 221. Elsevier.

GIBSON, C. H. 1982 On the scaling of vertical temperature spectra. *J. Geophys. Res.* **87**, 8031.

HELLAND, K. N. & VAN ATTA, C. W. 1978 The 'Hurst phenomenon' in grid turbulence. *J. Fluid Mech.* **85**, 573–589.

HINZE, J. O. 1975 *Turbulence*, 2nd edn. McGraw-Hill.

ITSWEIRE, E. C., HELLAND, K. N. & VAN ATTA, C. W. 1986 The evolution of grid-generated turbulence in a stably stratified fluid. *J. Fluid Mech.* **162**, 299–338.

LANGE, R. E. 1982 An experimental study of turbulence behind towed biplanar grids in a salt-stratified fluid. *J. Phys. Oceanogr.* **12**, 1506.

LIENHARD V, J. H. 1988 The decay of turbulence in thermally stratified flow. Doctoral dissertation, University of California, San Diego.

LIENHARD V, J. H. & VAN ATTA, C. W. 1989 Thermally stratifying a wind tunnel for buoyancy influenced flows. *Exps Fluids* (in the press).

LIN, T. J. & VEENHUIZEN, S. D. 1975 Measurements of the decay of grid-generated turbulence in a stratified fluid. *Flow Research Note no.* 85.

MÉTAIS, O. 1987 Turbulence submitted to stable density stratification and statistical theory. *Sixth Symp. Turbulent Shear Flows September 7–9. Toulouse.*

MÉTAIS, O. & HERRING, J. R. 1989 Numerical simulations of freely evolving turbulence in stably stratified fluids. *J. Fluid Mech.* **202**, 117–148.

MONTGOMERY, R. D. 1974 An experimental study of grid turbulence in a thermally-stratified flow. Doctoral Dissertation, University of Michigan.

OBUKHOV, A. M. 1949 Structure of the temperature field in a turbulent flow. *Izv. Akad. Nauk. SSSR, Ser. Geogr. i Geofiz.* **13**, 58–69.

RILEY, J. J., METCALFE, R. W. & WEISSMAN, M. A. 1981 Direct numerical simulations of homogeneous turbulence in density-stratified fluids. In *Nonlinear Properties of Internal Waves. AIP Conference Proc.* vol. **76**, pp. 79–112. American Institute of Physics.

SANDERSON, R. C., HILL, J. C. & HERRING, J. R. 1987 Transient behavior of a stably stratified homogeneous fluid. In *Advances in Turbulence* (ed. G. Comte-Bellot & J. Mathieu), p. 184. Springer.

SIRIVAT, A. & WARHAFT, Z. 1983 The effect of a passive cross-stream temperature gradient on the evolution of temperature variance and heat flux in grid turbulence. *J. Fluid Mech.* **128**, 323–346.

SREENIVASAN, K. R., TAVOULARIS, S., HENRY, R. & CORRSIN, S. 1980 Temperature fluctuations and scales in grid-generated turbulence. *J. Fluid Mech.* **100**, 597–621.

STEWART, R. W. 1969 Turbulence and waves in a stratified atmosphere. *Radio Sci.* **4**, 1269–1278.

STILLINGER, D. C. 1981 An experimental study of the transition of grid turbulence to internal waves in a salt-stratified water channel. Doctoral dissertation, University of California, San Diego.

STILLINGER, D. C., HEAD, M. J., HELLAND, K. N. & VAN ATTA, C. W. 1983*a* A closed-loop gravity-driven water channel for density-stratified shear flows. *J. Fluid Mech.* **131**, 73–89.

STILLINGER, D. C., HELLAND, K. N. & VAN ATTA, C. W. 1983*b* Experiments on the transition of homogeneous turbulence to internal waves in a stratified fluid. *J. Fluid Mech.* **131**, 73–89.

TAVOULARIS, S. & CORRSIN, S. 1981 Experiments in nearly homogeneous turbulent shear flow with a uniform mean temperature gradient. Part 1. *J. Fluid Mech.* **104**, 331–347.

VENKATARAMANI, K. S. & CHEVRAY, R. 1978 Statistical features of heat transfer in grid-generated turbulence: constant-gradient case. *J. Fluid Mech.* **86**, 513–543.

WISKIND, H. K. 1962 A uniform gradient transport experiment. *J. Geophys. Res.* **67**, 3033–3048.

YEH, T. T. & VAN ATTA, C. W. 1973 Spectral transfer of scalar and velocity fields in heated-grid turbulence. *J. Fluid Mech.* **58**, 233–261.